Title

Optical Coherence Tomography in Biofilm Research: A Comprehensive Review

Working title

OCT in Biofilm Research

Authors

Michael Wagner[1,2], Harald Horn[1]

[1] Karlsruhe Institute of Technology, Engler-Bunte-Institut, Chair of Water Chemistry and Water Technology, Engler-Bunte-Ring 9, 76131 Karlsruhe, Germany

[2] Karlsruhe Institute of Technology, Institute of Functional Interfaces, Hermann-von-Helmholtz-Platz 1, 76344 Eggenstein-Leopoldshafen

Corresponding authors

Michael Wagner (michael.wagner@kit.edu), Harald Horn (harald.horn@kit.edu)

phone: +49 721 608 42581

Abstract

Imaging of biofilm systems is a prerequisite for a better understanding of both structure and its function. The review aims to critically discuss the use of optical coherence tomography (OCT) for the visualization of the biofilm structure as well as its dynamic behavior. A short overview on common and well-known, established imaging techniques for biofilms such as scanning electron microscopy (SEM), confocal laser scanning microscopy (CLSM), Raman microscopy (RM), and magnetic resonance imaging (MRI) paves the way to imaging biofilms at the mesoscale, which is perfectly covered by means of OCT. Principle, resolution, imaging velocity and limitations of OCT are subsequently presented and discussed in the context of biofilm applications. Examples are provided showing the strength of this technique with respect to the visualization of the mesoscopic biofilm structure as well as the estimation of flow profiles and shear rates. Common and new structural parameters derived from OCT datasets are presented. Additionally, the review shows the importance of OCT with respect to a better description of mechanical biofilm properties. Finally, the implementation of multi-dimensional OCT datasets in biofilm modelling is shown by several examples aiming on an improved understanding of mass transfer at the bulk-biofilm interface.

Keywords

biofilm imaging, optical coherence tomography, structure, structural properties, structural templates, modelling

1 Introduction

Within the last three decades – since the Dahlem Conference in 1989 – the driving force of most of the biofilm research done worldwide is still the interest in understanding the interaction of structure and function of biofilms (Wilderer and Characklis, 1989). Once identified as the main place where microorganisms prefer to live or organize themselves, the interest in biofilms was no longer only driven by waste water treatment or fouling in technical systems but also by additional research fields (Costerton et al., 1994). For example, the role of biofilms in the environment has already been identified very early (Boyle and Scott, 1984) and is still a field for understanding the interaction of physical heterogeneity (i.e. structure) and function (Singer et al., 2010). Furthermore, the impact of biofilms on human health is still a highly attractive research area (Hall-Stoodley et al., 2004). A new emerging field is the understanding of biofilms as systems which can be used for production of valuable chemicals in biofilm reactors (Halan et al., 2012; Kiperstok et al., 2017; Sarkar et al., 2009). Currently it seems that for the part of biofilm function the locally resolved description of the activity within a certain biofilm structure is not completely satisfying. Micro sensors are only available for a limited number of relevant parameters such as dissolved oxygen, nitrous oxide, and ammonium (Boessmann et al., 2003; Bungay et al., 1969; Lv et al., 2015). The use of optodes in biofilm research is not fully developed although planar optodes reveal the concentration of i.e. dissolved oxygen at the interface optode-biofilm with a high spatial resolution (Haberer et al., 2011; Staal et al., 2011). Fluorescence *in situ* hybridization (FISH) will typically generate an image of the distribution of the targeted microorganisms after their inactivation (Nielsen et al., 2009). Surface-enhanced Raman scattering provides more detailed chemical information about the biofilm by addition of colloidal silver or gold nanoparticles (Ivleva et al., 2010b). However, nanoparticle addition might have an impact on the biofilm structure and function by itself.

On the other hand the identification of the biofilm structure can be realized with a wide variety of methods which analyze and/or image the local organization of the different components within a biofilm system as shown in the review of Neu et al. (2010). Partly these methods also deliver information on biofilm function. Beside the generation of three-dimensional (3D) imaging datasets the question on which scale tools and methods are applicable is important. This research question has been addressed by Morgenroth and Milferstedt (2009). Nevertheless, a clear definition of temporal and/or spatial scales is lacking. Two main scales seems to be important in biofilm research. For the activity and organization of single microorganisms the microscale is the one which should be observable with the applied methods. For the mechanical function and the physical interaction of biofilms with the surrounding fluid the mesoscale is of greater interest. The presented review will try to critically analyze whether optical coherence tomography (OCT) as the emerging image technique in biofilm research can be the method to throw more light on the mesoscale and in turn the understanding of fluid-structure interactions. Two topics will be analyzed: visualization and monitoring of the biofilm structure as well as the assessment of physical biofilm properties.

2 Established biofilm imaging techniques

As the 'size' of the biofilm may change over time or the interest in another scale is growing, different visualization modalities become more applicable. In Wagner et al. (2010) a scheme across the scales has been introduced (see Figure 1). Therein, the microscale is defined as the range of several 10 to 100 µm capturing single cells, (initial) biofilm aggregates, and developing biofilm patches with axial and lateral resolutions < 1 µm. The mesoscale has been proposed to cover several mm large biofilm structures. It was further suggested that the mesoscale provides a representative view since it contains repeating structural units (Milferstedt et al., 2008a; Wagner et al., 2010b). Achievable resolutions vary greatly between the different mesoscopic imaging techniques. Nevertheless, resolutions of several µm to several 10 µm are possible. The scale which covers areas of several hundred mm^2 or even cm^2 has been defined as macroscale. The macroscale will not be discussed in this review. Focus is paid to the micro- and mesoscale, because mass transport and transfer processes as well as fluid-structure interactions are occurring at these scales.

2.1 Imaging the microscale of biofilms

According to Ernst Abbe the smaller the wavelength the higher the lateral resolution (Abbe, 1873). Thus, scanning and transmission electron microscopy (SEM, TEM) are often applied to visualize initial biofilm formation starting with single cells attached to an interface in the aquatic environment (Bridier et al., 2013). To avoid irreversible alteration of the biofilm structure during sample preparation (see Figure 2) environmental scanning electron microscopy (ESEM) has been developed. ESEM allows analysis of biological samples (Priester et al., 2007) such as membrane fouling and scaling (Nguyen et al., 2012; Wibisono et al., 2015). As EPS provide less contrast in ESEM, contrast agents are often added prior to the visualization. A promising technique visualizing the microscale with a less invasive sample preparation (e.g., no contrast agents are required) is helium ion microscopy (HIM; Joens et al., 2013). Due to scanning the sample with an helium ion beam instead of an electron beam, HIM alters the sample structure less and generates high contrast images (Ward et al., 2006). Especially, at very high magnifications of > 150000 HIM does not show imaging artifacts (e.g., charging artifacts).

Interactions of high-energy photons and the sample results in spectroscopic information. SEM/TEM is hence often coupled to an energy dispersive X-ray analysis (EDX) to characterize exopolysaccharides of specific bacteria (Singh et al., 2011), map the distribution of nanoparticles inside biofilms (Reith et al., 2010), or to determine the elemental composition of deposit layers in membrane systems (Valladares Linares et al., 2014). However, Lawrence et al. (2003) assessed the constituents of the biofilm matrix by performing a near-edge X-ray absorption fine structure (NEXAFS) analysis which confirmed the presence of proteins, (poly)saccharides, lipids, and nucleic acids. The aforementioned methods all require some sample treatment which is more or less invasive, may to some extend alter

the biofilm structure, utilize highly specialized equipment (e.g., synchrotron radiation), and are available only at a limited number of labs worldwide.

Other methods have thus been developed which allow the *in situ* and non- or less-invasive characterization of the biofilm structure chemically and physically. Here Raman microscopy (RM) showed recently great potential. Probably the greatest advantage of this technique is that biofilms can be examined in their native, un-altered state: immersed into water. Without sample preparation information about the chemical nature of a biofilm is determined (Ivleva et al., 2010a). A single Raman spectra contains information about organic (polysaccharides, proteins, lipids, humic-like substances, etc.) as well as inorganic constituents (e.g., minerals; Pätzold et al., 2006) or (micro)plastics; Kniggendorf and Meinhardt-Wollweber, 2011). A comprehensive list can be found in (Ivleva et al., 2009). Based on a comprehensive Raman band assignment, specific signals can be extracted and mapped (semi-)quantitatively (Ivleva et al., 2009; Ivleva et al., 2010a; Kniggendorf et al., 2016).

Due to the low quantum efficiency scanning a biofilm area of several μm^2 will last hours. To speed-up the spectra acquisition, surface or tip enhanced Raman spectroscopy (SERS, TERS) has been introduced (Ivleva et al., 2010b; Neugebauer et al., 2006). Recent studies of Kubryk et al. (2015, 2016) revealed a red-shift of Raman signals in individual bacterial cells when stable isotope labeled substrates (^{13}C, ^{2}H) were fed to the biofilm. This methodology has clearly the potential to resolve metabolic pathways as well as can make use of 'modified' bacterial cells as bio-compatible tracers ('bio-tracers') in environmental studies (e.g., soil remediation).

The aforementioned techniques may or may not provide a graphical representation of the biofilm sample under investigation. As a consequence fluorescence microscopy is applied widely. More specifically, confocal laser scanning microscopy (CLSM) has become the 'work-horse' in biofilm research (Neu et al., 2010; Neu and Lawrence, 2015). CLSM is an optical sectioning technique which acquires fluorescence signals only from a few hundred nanometer thick focal plane within the sample (Minsky, 1988). Compared to normal or *epi* fluorescence microscopy this a significant advantage as the sample is now scanned in 3D point-by-point, section-by-section, slice-by-slice (Pawley, 2006). Meanwhile many derivates have been developed such as light sheet microscopy (Santi, 2011; Taormina et al., 2012) or spinning-disk systems (Lin and Scott, 2012). Even Abbe's law regarding the resolution limit has been 'passed-by' by the group of the Novel Price winner Stefan Hell (Hell, 2007; Hell, 2009). 'Nanoscopy' allows optical investigations far below the single cell level with incredibly high lateral resolutions < 10 nm (Berk et al., 2012).

This excursion shows the trend towards enhanced acquisitions speed and high-resolution fluorescence microscopy. Nevertheless, much understanding about biofilm composition and architecture (Chen et al., 2007; Neu and Lawrence, 2014) as well as their relation to mass transfer (Yawata et al., 2009) and metabolism is gained from rather simple CLSM point scanners. These are used to characterize biofouling layers (Bjørkøy and Fiksdal, 2009; Derlon et al., 2013), how bulk flow shapes the biofilm

structure (Besemer et al., 2007) and how higher organisms alter the biofilm structure (Peter-Varbanets et al., 2010). CLSM was also used to quantify the effect of cleaning procedures by West et al. (2014). Although fluorescence microscopic techniques and microscopes itself have been improved tremendously in the last decade, still the representativeness of the visualized biofilm structure depends on the applied fluorescent stains and their interactions with the biofilm. Bacteria – precisely, their nucleic acids – are stained with fluorochromes binding to RNA and DNA (i.e., SYTO dyes, SYBR dyes). Application of genetic techniques causing the expression of fluorescent proteins by bacteria are also feasible (Herzberg and Elimelech, 2007; Xi et al., 2006). Labeling the EPS matrix is rather difficult, because EPS are for most (multispecies) biofilms a complex mixture instead of a well defined polymer (Flemming et al., 2016; Flemming and Wingender, 2010). There is no universal stain which binds specifically to a certain polymer or unspecifically to all polymers. In 2003 Staudt et al. performed a lectin-binding analysis screening over 60 lectins for their binding affinity to the EPS of a heterotrophic wastewater biofilm. Their results unequivocally reveal that lectins only mark a certain fraction of the EPS. Nevertheless, biofilm researchers have to accept and tackle the uncertainty of fluorescence microscopy with respect to the visual representation of the biofilm as well as to quantitative results derived through image analysis (Beyenal et al., 2004b). As an example, Wagner et al. (2010) visualized the biofilm structure of a heterotrophic wastewater biofilm by means of CLSM and OCT. Comparison of CLSM and OCT results revealed substantial differences. As the study investigated the same biofilm with both methods, results highlight the uncertainty of CLSM measurements; namely lectin-binding specificity, fluorochrome penetration or expression, excitation/emission attenuation, quenching effects and more (Neu et al., 2010; Shotton, 1989; Wagner et al., 2009).

2.2 Imaging the mesoscale of biofilms

At the mesoscale bulk flow interacts with biofilm at the bulk-biofilm interface (fluid-structure interactions). It is further the scale at which the overall biofilm structure and distribution is assessed. Imaging the mesoscale of biofilms often employees stereo microscopy and magnetic resonance imaging. Compared to microscopic tools the field-of-view is enlarged and the spatial resolution is decreased. Stereo micrographs store morphological information in gray intensity levels (e.g., biofilm thickness: the thicker the biofilm, the lower the gray intensity). By applying sophisticated image analysis tools (i.e., SGLDM, see Haralick et al., 1973; Lee et al., 1992; Milferstedt et al., 2008b) to interpret the grayscale distribution structural features of the biofilm can be extracted and related to the growth conditions. Saur et al. (2016) visualized biofilm growing on transparent coupons in bubble column reactors by means of stereo microscopy (imaged area: 6.4 mm × 4.8 mm). Their methodology further allows to quantify moving predators, which are of interest in membrane systems as these organisms influence the filtration performance (Saur et al., 2014). Thereby, almost no or even no

sample pre-treatment is necessary allowing stereo microscopy to be used as a monitoring tool (Pons et al., 2008).

Ultrasound imaging and X-ray computed microtomography were also tested for imaging biofilm at the mesoscale (Davit et al., 2010; Shemesh et al., 2007). However, for the last decades magnetic resonance imaging/microscopy (MRI/MRM) was the preferred techniques to visualize the mesoscale of biofilms in all three spatial dimensions. Here, researchers make use of the high water content of biofilms (Callaghan, 1991). Normal water $^{1}H_2O$ contains protons ^{1}H which interact with magnetic fields and radio frequency pulses. Additionally, the relaxation behavior of $^{1}H_2O$ after a radio frequency excitation depends on the interaction with the surrounding matter (e.g., $^{1}H_2O$, EPS). Thereby, molecular contrast is generated which allows to separate 'free' water from 'bound' water stored inside the biofilm in 3D (Hornemann et al., 2008; Hoskins et al., 1999). Various studies resolved the flow profiles in all spatial directions in biofilm tube reactors (Manz et al., 2003; Manz et al., 2005; Nott et al., 2005). MRI/MRM also allows relating the shear stress at the bulk-biofilm interface to biofilm detachment events (Wagner et al., 2010a). Graf von der Schulenburg et al. (2008) applied MRM/MRI to assess the impact of growing biofilm inside membrane fouling simulators on the local hydrodynamic conditions. MRI/MRM does not suffer from penetration limitations as known for other imaging modalities (e.g., light microscopy). Hence, it is often applied to visualize biofilms within porous media (e.g., soils; (Hoskins et al., 1999)) as well as resolve transport phenomena (Baumann and Werth, 2005; Gjersing et al., 2005; Hornemann et al., 2009). In addition to transport of dissolved species (i.e., metal ions; McLean et al., 2008; Ramanan et al., 2010 and substrates; Renslow et al., 2014), nanoparticle transport, interaction with humic substances and deposition in porous media systems was studied recently (Cuny et al., 2015).

Beside the advantage of visualizing biofilm, free flowing water as well as solid and dissolved species simultaneously, MRI/MRM has some drawbacks (e.g., high administrative demand, long measurement times, and operational costs). Most critical to the authors of this review is the fact, that the size of the object (e.g., biofilm reactor) which will be investigated needs to fit into the bore of the MRI/MRM tomograph. Here diameters of more than 10 cm are very seldom. Moreover, the larger the object the lower the resolution. To achieve acceptable resolutions of 50 – 100 µm per length of the scanned volume units, biofilm reactors are often scaled down to a diameter of 25 mm or lower. The study conducted by Vrouwenvelder et al. (2009) nicely shows that MRI/MRM experiments require certain compromises: The membrane fouling simulator had to be constructed from PVC as (i) most metals cannot be used due to the interaction with the strong magnetic field as well as (ii) their shielding of electromagnetic radiation, and (iii) as PVC cannot withstand high pressures (≈ 10 bars), no permeate was produced.

3 OCT in biofilm research

This review thus tries to describe why optical coherence tomography might be the most suitable imaging tool for biofilms at the mesoscale. The working principle will be explained briefly, advantages and disadvantages as well as limitation will be discussed in the context of biofilm related publications.

3.1 Measurement principle, dataset composition, resolution

There are various text books which describe OCT in detail. For instance confer to Drexler and Fujimoto (2008) and Bouma and Tearney (2001). Furthermore, several review articles have been published explaining the physical and technical aspects (Fercher et al., 2010; Huang et al., 1991; Schmitt, 1999). For a basic understanding a brief explanation of the working principle is provided. OCT is an interferometric imaging technique. Having a classical Michelson-type interferometer in mind, there is a light source, a dichroic mirror (beam splitter), a reference arm of a constant or varying length, and a sample arm. The sample arm is equipped with an objective lens focusing at the sample (e.g., biofilm). Light of the light source is reflected and scattered by the sample causing interference with the light of the reference arm at the dichroic. This interference is digitally recorded and analyzed. As light sources lasers and super luminescent diodes are used providing low-coherence near-infrared light (coherence length of several µm) with good penetration characteristics in biological samples such as biofilms.

Of course, in modern devices fiber-optics replace the components of the Michelson interferometer allowing for the construction of compact, robust and movable devices. There are two main branches: time-domain (TD) and Fourier or spectral domain (SD) OCT. Recent developments allow both technologies for the high quality visualization of the biofilm structure (Yaqoob et al., 2005). Independent of whether TD- or SD-OCT is used, axial intensity profiles are acquired containing depth-resolved structural information about the analyzed sample. These axial profiles are referred to as ‘A-scan’. A series of A-scans represents an optical cross-section (xz-plane) which is named ‘B-scan’. Finally, a series of adjacent B-scans creates volume scan. This volume scan has not been named, yet. In ultrasound tomography a C-scan refers to a xy-plane of signals with identical traveling time. This also applies to OCT measurements; the xy-plane represents an *en-face* view. However, the authors of this review would like to use the term ‘C-scan’ to indicate a volumetric OCT dataset. Although, the name C-scan does not indicate the orientation of the imaging data, using A-scan for 1D, B-scan for 2D, and C-scan for 3D datasets is in a logical order and will support the understanding of OCT related publications. As this postulation will still be prone to discussion – especially with ophthalmologists – it is herewith recommended to indicate the orientation of OCT imaging data in publications.

Of similar importance is the correct reporting of the resolution of the acquired imaging datasets. Maybe due to a lack of knowledge, the physical resolution is mixed up with the pixel resolution. The first is defined by the optical components (e.g., light source, numerical aperture of the objective lens,

grating) and dispersing components in the light path whereas the second is user-defined in the software. Assuming the use of a Thorlabs GANYMEDE-II SD-OCT system (Thorlabs, Dachau, Germany) from the shelf equipped with an OCT-LK3-BB objective lens kit, it provides a central wavelength of 930 nm resulting in an axial resolution of 6 µm in air (refractive index $n = 1$) and a lateral resolution of 8 µm (values taken from GANYMEDE-II product page found at www.thorlabs.com, assessed 24 Nov 2016). In the OCT software the user is i.e. able to scan laterals of 5 mm length (x, y) by 1000 pixels each. This causes a pixel resolution of 5 µm/px and in turn represents a certain oversampling. More critical is the axial resolution. GANYMEDE-II systems provide a imaging depth range of 2.9 mm in air. These 2.9 mm are represented by 1024 pixel. Each pixel in axial direction equals a height of 2900 µm/1024 px = 2.83 µm/px in air. In water this pixel resolution is further 'improved' by the refractive index of water ($n = 1.333$ at 20°C) resulting in a pixel height Δz of 2.83 µm/px/1.333 = 2.12 µm/px. Thereby, selecting the correct refractive index becomes important. In consequence a careful reporting of the physical, optical, and pixel resolution is highly recommended and requires basic understanding of the physics behind OCT. This allows for more transparent research and would for instance trace the calculation of structural parameters; for instance biofilm thickness, roughness, and average horizontal run length. Reporting of different axial resolutions for similar devices (wavelength, bandwidth, objective lens kit) is confusing and misleading (compare Blauert et al. (2015) and Derlon et al. (2016)).

3.2 Biofilm structure and fluid-structure interaction

Since OCT detects reflection and scattering signals, it is well suited to visualize the overall distribution of particular matter in biofilms. More importantly the main limitation of especially fluorescence imaging is overcome: regions of background signals surrounded by biofilm are identified as voids and cavities (Valladares Linares et al., 2016; Wagner et al., 2010b). To date none of the biofilm research groups applying OCT have reported if these cavities contain other matters than water (e.g., EPS). However, due to the dependency of OCT from the refractive indices of the sample, voids containing matter of a refractive index different to water (e.g., gases) would cause a distortion in the image. As such observations have not been reported for biofilms yet, it is mostly likely to assume that signal free spaces inside biofilms are filled with water.

In the publication of Xi et al. (2006) and Haisch and Niessner (2007) OCT has firstly be shown to be capable of visualization the structure of biofilms non-invasively and *in situ*. Xi et al. (2006) monitored the growth of biofilm in a glass capillary. Haisch and Niessner (2007) already went a step further by separating low- and high-density parts of the biofilm structure based on the intensity of the OCT signal acquired using an in-house modified TD-OCT originally used for medical purposes. In 2010 Wagner et al. (2010b) were the first using a commercial SD-OCT (Thorlabs GANYMEDE-I system, Dachau, Germany) for the visualization of heterotrophic wastewater biofilms grown in a flume on objective slides (substratum). Although, biofilms of this study were thick (1.2 – 1.6 mm), a complete

visualization down to the substratum of the fully hydrated biofilm was achieved. Structural differences were obvious, represented by several structural parameters and connected to the hydrodynamic growth conditions. Results show that the compactness of a biofilm increases with the Reynolds number (see Figure 3). Most impressively is the fact that single OCT C-scans of 4 × 4 × 2.1 mm^3 (resolution < 20 µm/px) were acquired within 2 min without any sample pretreatment. Such volumes were beforehand analyzed using MRI/MRM, but at a fairly course resolution of ≈ 20 - 160 µm/px (Manz et al., 2003; Seymour et al., 2004; Wagner et al., 2010a).

Since the publications of Haisch and Niessner (2007) and Wagner et al. (2010b), OCT gained more and more attention in biofilm research. Meanwhile various groups used OCT to monitor the biofilm development and biofilm structure changes in complex/sophisticated cultivation setups. Especially, setups are investigated which are hardly to modify to fit a certain instrumentation such as CLSM, SEM, and MRI/MRM. Most recently, Fortunato et al. (2016) implemented an on-line OCT measurement in a gravity driven submerged membrane bioreactor to study the development of biofouling on the flat-sheet membrane. Over a period of 43 days they captured and quantified the change of the biofilm structure from a thin and porous biofilm (until day 10) towards a compact biofouling layer of 250 µm thickness. The results can be treated as valid, because the biofilm structure was visualized without alteration of the biofilm. Beside gravity driven membrane systems (Derlon et al., 2013; Derlon et al., 2016; Shen et al., 2015) high-pressure operated membrane systems such as reverse osmosis devices are technologically important. So-called membrane fouling simulators (MFS) are used to investigate the biofouling formation at lab-scale. Macroscopic pressure measurements (transmembrane pressure and feed channel pressure drop) provide a good indication of biofouling inside MFS. However, the impact of the local distribution of biofilm inside the MFS was invasively assessed through a membrane autopsy. This restriction was overcome by Dreszer et al. (2014) using a MFS with a partially transparent lid. Monitoring by means of OCT revealed biofilm development inside the feed channel at a constant flux of 20 L/(m^2 h). Within five days the biofilm thickness reached 200 µm leading to a hydraulic biofilm resistance of 8×10^{12} m^{-1}. However, as only scans of 10 mm × 0.008 mm were acquired local variations of the biofilm structure were not addressed. Such simplifications might be tolerated when no feed spacer is installed in the feed spacer channel of the MFS. But as the biofouling in (reverse osmosis) membrane modules is massively influence by the feed spacer, MFS experiments need to apply feed spacers (Vrouwenvelder et al., 2009). West et al. (2016) manufactured a MFS with optical windows in the lid to conduct a most realistic testing scenario for two different feed spacers and two different feeds. Their study visualized the accumulation of biofilm on the membrane surface as well as at the feed spacer within C-scans of 7 × 7 × 1.2 mm^3. The results clearly confirm that (i) the feed spacer is markedly influencing the fouling behavior as well as that (ii) imaging tools such as OCT are necessary to understand differences among experimental parameters (e.g., feed and feed spacer geometry). A similar approach was recently published by Fortunato et al. (2016a). Working with feed spacers is challenging with respect to image analysis. For instance, West

et al. (2016) had to assure an accurate quantification of biofilm related signals independent of the abundance of signals allocated to the feed spacer. OCT analysis could in future thus confirm and prove simulation approaches propagated recently by Siddiqui et al. (2016) as strategy for the optimization of feed spacer geometries.

Due to the non-invasivity, ease-of-use and acquisition speed OCT might be applied in other testing scenarios more regularly. A suitable field of application includes the evaluation of cleaning procedures. The cleaning efficiency of chemicals is often determined macroscopically based on flux measurements (Ang et al., 2006) as well as ATP and carbohydrate analyses (Hijnen et al., 2012). In some studies microscopic tools are used the assess structural changes of the fouling deposits (West et al., 2014). However, a more general picture is assessable by applying OCT. Rasmussen et al. (2016) applied cross-polarization OCT and resolved the penetration behavior of chlorhexidine in artificial oral biofilms over time.

Removal of biofilm is triggered by the destabilization of the biofilm matrix as well as by the forces acting on the biofilm structure. Detachment occurs when the shear force exceeds the cohesive strength of a biofilm. To determine the shear forces, velocity gradients need to be quantified. This is either done through simulations, particle imaging velocimetry, or measurements using MRI/MRM approaches (Graf von der Schulenburg et al., 2008; Stewart, 2012; Wagner et al., 2010a). The restrictions of MRI/MRM have already been mentioned. Thus, the OCT approach of Gao et al. (2013) sounds promising. They characterized the axial velocity profile at the different locations within a feed spacer filled MFS. This group further extended their methodology to assess the development of the fouling layer from Doppler OCT measurements (Gao et al., 2014). Recently, a sophisticated approach was presented by Weiss et al. (2013) who calculated the longitudinal as well as transversal velocities from the alteration of the OCT signal in a flowing colloidal suspension. They determined the parabolic flow velocity profile in a cylindrical capillary (I.D. ≈ 600 µm) at laminar flow with pixel resolutions of ≤ 11 µm/px. Hence, multi-dimensional information about the velocity and subsequently about the shear stress distribution becomes available through OCT at resolutions 3- to 10-times better compared to MRI/MRM (see Wagner et al. (2010a)). In addition to the flow, the distribution of biofilm and shear stress inside a flow cell is accessible, can be visualized, and quantified as shown by Weiss et al. (2016). Moreover, the diffusion coefficient of suspended particles (e.g., polystyrene spheres) can be determined (Weiss et al., 2015).

3.3 Estimation and modelling of biofilm characteristics

In the previous section the various fields of applications for OCT in biofilm research were presented. The versatile use of OCT became obvious. However, in addition to a pure visualization of the biofilm structure, measures are required allowing for the objective comparison of imaging datasets as well as a statistical treatment of available data. The following part of this review will report about OCT dataset treatment and common structural parameters used to describe the biofilm structure.

3.3.1 Structural properties

Except of velocity determinations as performed by Weiss et al. (2013; 2016), most parameters used to describe the investigated biofilm (system) are calculated from binary image datasets. Hence, parameters calculated from CLSM, MRI/MRM, and other tomography datasets can also be derived from OCT datasets. Available software tools (e.g., PHLIP, COMSTAT, ISA 2D/3D; for more details see Neu and Lawrence (2015)) might also be used to analyze OCT datasets. A comprehensive list of structural parameters has been presented a decade ago by Beyenal et al. (2004a) who also discussed – similar to other studies – the meaning and quality of structural parameters (Beyenal et al., 2004b). Since CLSM is widely applied, a comparison of biofilm structure has thus been performed predominately at the microscale. Additionally, the meaning and quality of individual parameters has been discussed in the context of e.g. incomplete staining and limited penetration depth. Nevertheless, common parameters used to quantify the biofilm structure are: (mean) biofilm thickness, roughness, roughness coefficient, porosity, volumetric coverage, fractal dimension, biovolume, and run length. In addition to these parameters, OCT C-scans can be converted into topographic representations of the bulk-biofilm interface. By analyzing the topography using methods such as SGLDM (Pons et al., 2008) or those available as plugins (i.e., SurfaceJ by Chinga et al., (2007) for ImageJ (Schindelin et al., 2012), the number of structural parameters becomes extended by textural descriptors (Milferstedt et al., 2008b).

Binarization

To separate the biomass related signals from those of background noise is the most crucial step in analyzing OCT datasets. Follow-up procedures are affected by this separation based on a certain threshold. It shall not be discussed what the ‘right’ thresholding algorithm is. Often the Otsu method is used (Otsu, 1979; Yerly et al., 2007). Some groups used the ‘triangle’ algorithm (Derlon et al., 2013) or judged their imaging datasets manually (Blauert et al., 2015). However, attempts exist which try to optimize the thresholding by minimizing the error (Kittler et al., 1985; Kittler and Illingworth, 1986) or by implementing more robust techniques (Xavier et al., 2001). Independent of the thresholding method chosen, the separation into fore- and background is performed by interpreting the grayscale/intensity distribution either in a single B-scan or within a C-scan. Although, most OCT used in biofilm research are spectrometer-based SD-OCT systems, less or even no attention is paid to the variation of the signal-to-noise ratio (SNR) over depth. This SNR drop-off increases with the difference in length between the reference and sample arm as described coherent in Yaqoob et al. (2005). This drop-off should not be neglected as it may reach 20 decibel (dB) (Yaqoob et al., 2005). To avoid the drop-off influencing the thresholding, it is recommended by the authors of this review to binarize OCT datasets as illustrated in
Figure 5. In Figure 5 (A) the SNR drop-off influences the correct recognition of biofilm, because the thresholding algorithm judges between fore- and background including the SNR drop-off. Thus,

405 binary images after applying the Otsu and triangle algorithm differ. On the contrary, binarization
406 performed using Otsu's method following the scheme proposed in Figure 5 (B) leads to a complete
407 detection of biofilm. Consequently, the binarization quality depends on the thresholding algorithm as
408 well as on the orientation of OCT imaging data.
409 In addition, applying filters (e.g., mean or median) prior to the thresholding may help to achieve good
410 binarization results. However, filters alter the imaging data. Care should thus be paid to avoid
411 significant alteration of the structural information of the biofilm, which is subsequently quantitatively
412 described using structural parameters.
413
414 **Biofilm thickness and mean biofilm thickness**
415 As OCT datasets cover a large scan area of several mm^2 the mean biofilm thickness is calculated to
416 quantify the visualized biofilm. However, there are several ways to define and calculate the mean
417 biofilm thickness.
418 The first attempt distributes all foreground (biofilm) signals of a binary 3D dataset evenly above the
419 scanned area. The mean biofilm thickness is calculated according to

$$\bar{L}_F = \frac{V(1)}{A} \quad (1)$$

420 wherein $V(1)$ equals the volume covered by foreground/biofilm signals and A is the analyzed basal
421 area. The mean biofilm thickness calculated that way is comparable to gravimetrical determinations.
422 Using this method, heterogeneities within the biofilm structure are homogenized.
423 The following approach accounts for the spatial distribution of biomass and cavities within biofilms as
424 well as for irregularities of the bulk-biofilm interface. Hence, is the preferably used method to
425 calculate the mean biofilm thickness. In general, the biofilm thickness L_F is the distance between the
426 substratum and a point at the bulk-biofilm interface perpendicular to the substratum. The mean biofilm
427 thickness is hence calculated as follows

$$\bar{L}_F = \frac{1}{N}\sum_{i=1}^{N} L_{F,i} \quad (2)$$

428 where $L_{F,i}$ is a local biofilm thickness measurements at location *i* and N equals the number of
429 thickness measurements (if a complete C-scan is analyzed, N is equal to the number of A-scans).
430 It is important to stress, that a correct calculation of the (mean) biofilm thickness depends on the right
431 selection of the voxel/pixel height Δz. It depends on the refractive index of the media within the
432 optical path and is defined as

$$\Delta z = \frac{\Delta z_{air}}{n} \quad (3)$$

433 with n being the refractive index of the penetrated media, Δz being the effective axial resolution in
434 this medium and Δz_{air} being the axial resolution of the device in air ($n = 1$, Bouma and Tearney,
435 2001). From Eq. 3 it can be derived that the higher the refractive index, the better the axial resolution.
436 As OCT devices and software tools (e.g., ImageJ/Fiji, Schindelin et al., 2012) to date do only allow to

437 set a single refractive index for the complete dataset, the refractive index of a biofilm is assumed to be
438 $n = 1.333$ (20°C) equal to that of water (Blauert et al., 2015; Dreszer et al., 2014; Fortunato et al.,
439 2017; Shen et al., 2016; Wagner et al., 2010b). This might be an acceptable assumption for an
440 unaltered, sponge-like biofilm structure containing a high fraction of water. But when the biofilm is
441 compressed (Valladares Linares et al., 2016) this simplification becomes to some extend obsolete the
442 more water is released. However, Ratheesh Kumar et al. (2015) estimated the refractive index of
443 biofilm during a cultivation by means of a swept-source OCT. Their measurements revealed a
444 refractive index of $n \approx 1.355$ confirming the general simplification made in most studies. However,
445 they did not evaluated the change of the refractive index during a compression experiment.
446
447 Using Eq. 2, Wagner et al. (2010b) determined a mean biofilm thickness of 1.3 – 1.6 mm for a
448 heterotrophic wastewater biofilm grown in a lab-scale flume. Such high values have previously only
449 be reported from MRI/MRM experiments by Manz et al. (2005). Thin biofilms of 30 – 40 µm were
450 analyzed on membranes (Shen et al., 2016). OCT was also used to reveal how grazers in an
451 oligotrophic environment control the mean biofilm thickness in a range of 50 – 250 µm. In the study
452 of Rasmussen et al. (2016) a 15 min exposure to urea caused an increase of the biofilm thickness
453 (approx. 500 µm at t = 0) by ≈ 40%. Thickness measurements were also conducted to evaluate the
454 compression behavior of biofilms (Blauert et al., 2015). Valladares Linares et al. (2015) monitored the
455 compression-relaxation characteristics of biofilm cultivated in a MFS in a series of B-scans ($\bar{L}_F \approx$
456 $200 - 300\mu m$). A flux increase by 200% led to a reduction of the mean biofilm thickness by 40%.
457 Subsequent flux reduction to the initial level did not cause a full recovery of the biofilm structure.
458
459 **Roughness and roughness coefficient**
460 Roughness in general describes surface properties. According to Nowicki (1985) there are several
461 parameters feasible as roughness measures. The common descriptors used in biofilm research are
462 roughness and the roughness coefficient. Both parameters describe the smoothness of the biofilm
463 surface/bulk-biofilm interface. Roughness R_a quantifies the absolute variation to the biofilm thickness
464 according to Eq. 4.

$$R_a = \frac{1}{N}\sum_{i=1}^{N}\left|L_{F,i} - \bar{L}_F\right| \tag{4}$$

465
466 For comparing the structure of different biofilms, across different studies as well as across scales, the
467 roughness coefficient R_a^* was introduced by Murga et al. (1995). It normalizes to roughness R_a to
468 mean biofilm thickness $\bar{L}_F$ (see Eq. 5).

$$R_a^* = \frac{1}{N}\sum_{i=1}^{N}\frac{\left|L_{F,i} - \bar{L}_F\right|}{\bar{L}_F} \tag{5}$$

469

One major advantage of OCT over other imaging techniques for biofilms is the high penetration depth. Biofilms are most often visualized completely. However, shadowing effects might occur (Derlon et al., 2013). Moreover, OCT datasets do not suffer from an incomplete visualization of the bulk-biofilm interface due to unstained constituents as knows for fluorescence methods (e.g., CLSM). Hence, roughness coefficients calculated from OCT datasets are expected to be representative and valid – at the very least when the axial resolution is set correctly as discussed earlier. Derlon et al. (2012) for example evaluated the biofilm surface roughness for their OCT datasets, but omitted the calculation for the additionally acquired CLSM stacks. In their study a low concentration of grazing eukaryotes caused the development of a smooth biofilm with a low roughness coefficient of $R_a^* = 0.25$. Elevated grazer concentrations (natural and doped level) increased the irregularity of the bulk-biofilm interface and in turn the roughness coefficient to 0.5 and 0.75, respectively.

Fluctuations of the flow velocity (e.g., shear stress) may also induce a change of the biofilm structure. Within their shear stress experiment, Blauert et al. (2015) observed a slight increase of the roughness coefficient from 0.18 to 0.24 within 2.1 s after the shear stress was increased. This might be contradictory to a general understanding of biofilm deformation, but revealed local differences in the deformation behavior. These findings thereby hint on a heterogeneous distribution of biofilm material properties.

Porosity

Porosity is another important structural parameter taking irregularities within the biofilm into account. And again, there are different approaches for the calculation available. Those approaches are not necessarily named different. Independent of the way of calculation, porosity is in accordance to Eq. 6 the ratio of void voxels [$voxels(0)$] over the overall number of analyzed voxels [$voxels(0) + voxels(1) = voxels(0,1)$]. The biomass is represented by the foreground [$voxels(1)$].

$$\Phi = \frac{\sum voxels(0)}{\sum voxels(0) + \sum voxels(1)} = \frac{\sum voxels(0)}{\sum voxels(0,1)} \quad (6)$$

Because porosity was calculated across scales between CLSM and OCT datasets, Wagner et al. (2010b) used the 'simplest' approach. In their study $voxels(0,1)$ was equal to the overall number of voxels in the C-scan ($L \times W \times H$, L = length, W = width, H = height). Thus, background signals [$voxels(0)$] above the bulk-biofilm interface contribute to the porosity of the biofilm and may lead to an overestimation as illustrated in

Figure 6 (A). However, as CLSM datasets did not allow to determine the bulk-biofilm interface completely it was the authors' only chance to compare the biofilm structure determined by means of CLSM and OCT. We suggest to call this the global porosity Φ_{global}.

$$\Phi_{global} = \frac{\sum voxels(0)}{\sum voxels(0,1)} = \frac{\sum voxels(0)}{L \times W \times H} \quad (7)$$

As porosity is intended to describe the internal biofilm structure, its calculation should discard void/background pixels/voxels above the bulk-biofilm interface. Hence, a complete detection/visualization of the bulk-biofilm interface as well as of the substratum are prerequisites (see Figure 6 (B)). Shadowing effects as obvious in the study of Derlon et al. (2013) may hinder the visualization of the substratum and thus cause additional post-processing. Biofilm porosity Φ_F is then calculated as follows:

$$\Phi_F = \frac{\sum voxels(0)}{\sum voxels(0,1)} = \frac{\sum voxels(0)}{L \times W \times \bar{L}_F} \quad (8)$$

where $\sum voxels(0,1)$ represents the total number of voxels beneath the bulk-biofilm interface. However, in the presence of bended, overlapping structures the biofilm porosity Φ_F might artificially be increased as depicted in
Figure 6 (C).
Nonetheless, porosity is an easy to understand and to interpret structural parameter. Compression of the biofilm structure due to shear forces acting at the biofilm surface may increase or decrease the porosity. Furthermore, the visual impression of the biofilm structure is resembled in this parameter. This is nicely shown by Fortunato et al. (2017) who observed an increase in the homogeneity of the biofilm structure and thus the decrease of its porosity Φ_F with ongoing operation of their membrane biofilm reactor; Φ_F decreased from 0.20 at day 5 to almost zero from day 15 forth.
Moreover, porosity is directly connected to transport processes within and through the biofilm. Derlon et al. (2012) as well as Fortunato et al. (2017) used biofilm porosity Φ_F to calculate the filtration resistance of the biofilm growing on the membranes.

Analysis of the bulk-biofilm interface

OCT allows complete visualization of the bulk-biofilm interface. In turn, the structural characterization of the biofilm surface over a large, representative area becomes possible. Several descriptors proposed by Nowicki (1985) might also be used to characterize the biofilm surface structure in more detail (e.g., by means of skewness or kurtosis).
But most important seems to be the calculation of the biofilm surface area as this is directly coupled to the utilization of substrates and nutrients from the bulk phase. Moreover, a change of the surface structure should influence the hydrodynamic conditions.
In addition to the absolute biofilm surface area, the surface enlargement factor (Picioreanu et al., 1998) can be calculated as done by Wagner et al. (2010) from MRI datasets.
Assessing the surface area of a biofilm, binarized OCT C-scans need to be reorganized in a way that the 3D dataset is presented as a series of xy-planes. In ImageJ this function is called ‘Reslice…’. The

thickness of such a xy-plane equals Δz. Assuming the visualization of the substratum, the distance h_i between the substratum and a particular xy-plane can be calculated and addressed as intensity to the entire xy-plane according to Eq. 9:

$$h_i = \frac{i \cdot \Delta z}{255} \tag{9}$$

where i equals the i-th xy-plane above the substratum (at the substratum $i = 0$); 255 is the intensity of a foreground signal in a 8-bit binary dataset. As the calculated distances h_i are floating point numbers, it is necessary to change the bit depth of the target dataset of xy-planes to 32-bit.

Finally, a maximum intensity projection generates the topographic representation of the biofilm surface/bulk-biofilm interface. The intensity variation equals the height variation and allows extraction of surface parameters such as the surface enlargement using for example the SurfaceJ plugin of ImageJ (Chinga et al., 2007). The entire approach is depicted in
Figure 7.

To the authors knowledge there is only the publication of Wangpraseurt et al. (bioRxiv) who introduced this approach describing the expansion and compaction of coral tissue. A change of the surface area by a factor of two was determined.

3.3.2 Mechanical properties

Mechanical properties of biofilms are still one of the blind spots in biofilm research. A major reason is the lack of applicable methods for the determination of relevant parameters which are the Young's modulus, shear modulus, adhesive or tensile strength. Very good reviews have been published on the available methods within the last 5 years (Billings et al., 2015; Böl et al., 2012; Guelon et al., 2011; Peterson et al., 2015). These reviews describe the main problems in determining relevant mechanical parameters. The most important problem is that biofilm samples cannot easily be transferred to the measuring device without altering/manipulating the desired properties. Biofilms are in some cases extremely thin, so that they cannot be transported to a measuring device at all. In general the best way would be to measure the characteristics in place without disturbing the biofilm sample.

Stress-strain analyses have been measured from compression experiments in a rheometer and have then been used to calculate the apparent Young's modulus, yield strength, and shear modulus (Körstgens et al., 2001). A common way is meanwhile to apply hydrodynamic shear stress and observe the deformation with a microscope. This has been done with light microscopy by Mathias and Stoodley (2009) as well as Galy et al. (2012). The authors stated that their methods could be further developed, respectively, optimized by acquisition of 3D time-lapsed images of biofilm structures under changing shear. For the latter case CLSM imaging is still much to slow to deliver enough data for the calculation of mechanical properties (Peterson et al., 2015).

Here, OCT offers the chance to overcome the lack of suitable and fast imaging technique. Blauert et al. (2015) have been the first to show the power of OCT imaging for the estimation of the shear modulus and Young's modulus. The extremely fast imaging capability allows for the acquisition of 2D videos in 'real-time' (Blauert et al., 2015; Valladares Linares et al., 2016) and time-lapsed 3D imaging (Blauert et al., 2015) showing overall biofilm deformation. The latter is exactly what is needed for the establishment of a fast and reliable method to determine mechanical biofilm properties.

Nevertheless, we are still far away from having the tools straight. Blauert et al. (2015) did the estimations of the biofilm material properties manually (see Figure 8) and tested only a few biofilm samples. In future, the imaging process has to be implemented into a tool chain to derive mechanical parameters objectively without user interaction. As pointed out by Mathias and Stoodley (2009) observing the same spot moving or shifting under the pressure of a changing hydrodynamic field is necessary. Furthermore, the resolution in time space depends on the A-scan rate of the OCT device. The higher it is, the more B-scans can be acquired per time unit. Hence, image artifact for example caused by oscillating biofilm structures are reduced. However, an increase of the scanning speed often causes the decrease of the signal-to-noise ratio.

Another example of the advanced use of OCT in this field is the study of Valladares Linares et al. (2015). In membrane filtration not only a parallel flow induces a force to a biofilm fouling layer, but also the vertical movement of water flowing through the biofilm and finally through the membrane, i.e. the permeate flux. The authors used OCT imaging to show the impact of changing flux on the biofilm structure (see Figure 9). The biofilm is compressed with the increase of flux and did not regain its original structure after decreasing the flux. With respect to the mechanical biofilm properties the authors found a higher velocity for the compaction compared to the relaxation process and a larger stiffness of the biofilm structure after compaction.

To stress the importance of OCT for this experiment it has to be clear that for instance CLSM cannot be used as the membrane fouling simulator is operated under pressure (1.7 bar) and that the most of the automated microscopes cannot handle such heavy loads ($m > 500$ g).

A recent manuscript describes an additional advantage of OCT: The parallel measurement of biofilm structure and flow field in microfluidic channels (Weiss et al., 2016). Back in 2013 the group already showed the possibility to measure the transverse and longitudinal flow velocities with OCT (Weiss et al., 2013). In their recent manuscript the authors demonstrate that the flow field or better the locally resolved shear rate does have an impact on biofilm growth (Weiss et al., 2016). That is in itself not new, the innovation is that both biofilm structure and shear rates are measured simultaneously using the same device.

3.3.3 Coupling OCT datasets to modelling approaches

Mainly the biofilm images which have been created by means of CLSM in the 1990`s pushed the approaches by which the structure and function of biofilms have been simulated in multi-dimensional biofilm models (Horn and Lackner, 2014). Furthermore, CLSM images have been directly implemented in simulation tools to show the relation between microscopic biofilm structures on the one hand and shear forces on the other (Böl et al., 2009). Another example is a finite-element study of *Staphylococcus aureus* released from a suture by tension, torsion, and bending studied by Limbert et al. (2013). The authors used the CLSM images to feed the model with real observed biofilm structures. As mentioned earlier, CLSM has disadvantages compared to OCT; mainly these are the time consuming imaging process and the visualization of only the stained/(auto)fluorescent biofilm parts. In case biofilm structures have to be implemented into biofilm models on the mesoscopic scale the application of by OCT generated images does make sense. Especially, for processes such as mass transfer at the bulk-biofilm interface and the fluid-structure interaction multi-dimensional OCT images seemed to be the right way to achieve an improved understanding. For the latter process, OCT might be able to deliver more than only the biofilm structure (Gao et al., 2013). The authors managed to visualize and measure the velocity field around a feed spacer by applying and analyzing the Doppler effect.

Martin et al. (2014) recently used biofilm structures which have been generated from OCT measurements for the simulation of permeate flux in a gravity-driven membrane system (GDM). Such systems somehow depend on the formation of biofilms above the membrane to stabilize the permeate flux over a long time of operation (confer to Derlon et al., 2013). The authors could show that by using the real, heterogeneous biofilm surface structure a better fit with measured permeate flux was achieved compared to a simulation assuming an average biofilm thickness.

Another direct implementation of 2D biofilm structures visualized by means of OCT into a simulation tool was presented by Li et al. (2015). Within this study, biofilm on a carrier material from a MBBR (moving bed biofilm reactor) was imaged and applied to simulate different flow conditions for understanding the interaction between biofilm structure and substrate turnover. Although complete 2D cross-sections (B-scan) of the carrier and biofilm were used, still a rigid biofilm structure was assumed for simplification. Especially, the movement of biofilm structures may play in future a larger role in biofilm models as indicated by Taherzadeh et al. (2012). As shown by Blauert et al. (2015) and Wangpraseurt et al. (bioRxiv) such interactions can be covered by means of OCT.

Fortunato et al. (2017) also simulated the permeate flux in a GDM system. As already done by Martin et al. (2014) the authors used the OCT B-scans to simulate the flux of water through biofilm layers developing on membranes (

Figure 10). Their manuscript does focus on the flow field and the resulting pressure at the bulk-biofilm interface. The heterogeneity of the biofilm surface significantly influences the flux of permeate. The authors do stress that in future the movement of the biofilm structure has to be incorporated into

models. However, the authors left open whether a rigid structure provides enough data for realistic simulations.

3.4 Concluding remark

Optical coherence tomography is the emerging imaging technique of the last decade in biofilm research. Its remarkable features are the fast – up to real-time – acquisition of multi-dimensional datasets, the *in situ* application as well as the fact, that no sample preparation is necessary allowing for a non-invasive and complete characterization of an unaltered biofilm structure. Additional advantages are the compact dimensions and mobility of on OCT device, which allows investigating biofilms directly inside the cultivation device (e.g., biofilm reactor) under operational conditions (e.g., flow). Hence, biofilms in various systems are analyzed, which are not accessible by other, established imaging modalities. Two- and three-dimensional datasets contain a representative description of the overall biofilm structure at the mm-scale (mesoscale) with µm-resolution. The structural descriptors are directly related to the shear and nutritional conditions of the experiment. Thus, the fundamental understanding of the fluid-structure interaction of biofilm systems can be further improved through coupling OCT imaging (e.g., biofilm structure and hydrodynamics) to multi-dimensional modelling approaches using commercial software packages.

A major step forward in biofilm research has been achieved by monitoring the deformation (e.g., compaction, relaxation) of the biofilm structure at real-time in a series of B-scans. In defined deformation experiments performed directly within the cultivation device (e.g., micro-fluidic flow channel), mechanical properties such as the shear and Young's modulus have thereby been determined non-invasively. This will in future definitely lead to a better understanding of fluid-structure interactions and further reveal the impact on mass transport and transfer characteristics.

However, OCT suffers – similar to other visualization tools – from limitations. For instance these are changing refractive indices along the z-axis, artifacts created by moving structures, or the signal-to-noise drop-off along an A-scan of SD-OCT devices. Although, OCT provides extraordinary penetration capabilities even in highly scattering biofilm samples, optical clearing agents might be necessary to be added in some experiments. Analysis of OCT datasets is affected more or less by one or more of these issues. In consequence, a common image analysis protocol is hitherto lacking and individual biofilm research groups develop custom procedures. In future, software developers for OCT devices may consider this fact.

Lastly, OCT does only provide information about the distribution of scattering and reflecting biofilm components. Neither cavities within biofilms have been identified as regions filled only with water nor are biofilm constituents resolved. Hence, biofilm composition and activity is not covered applying this tool. In future, molecular contrast experiments might be part of routine OCT analysis, but to date the combination with other imaging modalities such as CLSM and Raman microscopy is still necessary to reveal i.e. the abundance of bacteria within the EPS matrix.

4 References

Abbe E. 1873. Beiträge zur Theorie des Mikroskops und der mikroskopischen Wahrnehmung. *Arch. für Mikroskopische Anat.* **9**:413–418.

Ang WS, Lee S, Elimelech M. 2006. Chemical and physical aspects of cleaning of organic-fouled reverse osmosis membranes. *J. Memb. Sci.* **272**:198–210.

Baumann T, Werth CJ. 2005. Visualization of colloid transport through heterogeneous porous media using magnetic resonance imaging. *Colloids Surfaces A Physicochem. Eng. Asp.* **265**:2–10.

Berk V, Fong JCN, Dempsey GT, Develioglu ON, Zhuang X, Liphardt J, Yildiz FH, Chu S. 2012. Molecular architecture and assembly principles of Vibrio cholerae biofilms. *Science* **337**:236–239.

Besemer K, Singer G, Limberger R, Chlup AK, Hochedlinger G, Hödl I, Baranyi C, Battin TJ. 2007. Biophysical controls on community succession in stream biofilms. *Appl. Environ. Microbiol.* **73**:4966–4974.

Beyenal H, Donovan C, Lewandowski Z, Harkin G. 2004a. Three-dimensional biofilm structure quantification. *J. Microbiol. Methods* **59**:395–413.

Beyenal H, Lewandowski Z, Harkin G. 2004b. Quantifying Biofilm Structure: Facts and Fiction. *Biofouling* **20**:1–23.

Billings N, Birjiniuk A, Samad TS, Doyle PS, Ribbeck K. 2015. Material properties of biofilms—a review of methods for understanding permeability and mechanics. *Reports Prog. Phys.* **78**:036601 (17pp).

Bjørkøy A, Fiksdal L. 2009. Characterization of biofouling on hollow fiber membranes using confocal laser scanning microcscopy and image analysis. *Desalination* **245**:474–484.

Blauert F, Horn H, Wagner M. 2015. Time-resolved Biofilm Deformation Measurements using Optical Coherence Tomography. *Biotechnol. Bioeng.* **112**:1893–1905.

Boessmann M, Staudt C, Neu TR, Horn H, Hempel DC. 2003. Investigation and Modeling of Growth, Structure and Oxygen Penetration in Particle Supported Biofilms. *Chem. Eng. Technol.* **26**:219–222.

Böl M, Ehret AE, Bolea Albero A, Hellriegel J, Krull R. 2012. Recent advances in mechanical characterisation of biofilm and their significance for material modelling. *Crit. Rev. Biotechnol.* **8551**:1–27.

Böl M, Möhle RB, Haesner M, Neu TR, Horn H, Krull R. 2009. 3D finite element model of biofilm detachment using real biofilm structures from CLSM data. *Biotechnol. Bioeng.* **103**:177–186.

Bouma EB, Tearney JG. 2001. Handbook of Optical Coherence Tomography. Ed. E B Bouma 1st ed. New York: Marcel Dekker 756 p.

Boyle JD, Scott JA. 1984. The role of benthic films in the oxygen balance in an East Devon river. *Water Res.* **18**:1089–1099.

Bridier A, Meylheuc T, Briandet R. 2013. Realistic representation of Bacillus subtilis biofilms

718 architecture using combined microscopy (CLSM, ESEM and FESEM). *Micron* **48**:65–69.
719 Bungay HR, Whalen WJ, Sanders WM. 1969. Microprobe techniques for determining diffusivities and
720 respiration rates in microbial slime systems. *Biotechnol. Bioeng.* **11**:765–772.
721 Callaghan PT. 1991. Principles of Nuclear Magnetic Resonance Microscopy. *Med. Phys.* Vol. 19
722 1121p.
723 Chen MY, Lee DJ, Tay JH. 2007. Distribution of extracellular polymeric substances in aerobic
724 granules. *Appl. Microbiol. Biotechnol.* **73**:1463–1469.
725 Chinga G, Johnsen PO, Dougherty R, Berli EL, Walter J. 2007. Quantification of the 3D
726 microstructure of SC surfaces. *J. Microsc.* **227**:254–65.
727 Costerton JW, Lewandowski Z, DeBeer D, Caldwell D, Korber D, James G. 1994. Biofilms, the
728 Customized Microniche. *J. Bacteriol.* **176**:2137–2142.
729 Cuny L, Herrling MP, Guthausen G, Horn H, Delay M. 2015. Magnetic resonance imaging reveals
730 detailed spatial and temporal distribution of iron-based nanoparticles transported through water-
731 saturated porous media. *J. Contam. Hydrol.* **182**:51–62.
732 Davit Y, Iltis G, Debenest G, Veran-Tissoires S, Wildenschild D, Gerino M, Quintard M. 2010.
733 Imaging biofilm in porous media using X-ray computed microtomography. *J. Microsc.*
734 Derlon N, Grütter A, Brandenberger F, Sutter A, Kuhlicke U, Neu TR, Morgenroth E. 2016. The
735 composition and compression of biofilms developed on ultrafiltration membranes determine
736 hydraulic biofilm resistance. *Water Res.* **102**:63–72.
737 Derlon N, Koch N, Eugster B, Posch T, Pernthaler J, Pronk W, Morgenroth E. 2013. Activity of
738 metazoa governs biofilm structure formation and enhances permeate flux during Gravity-Driven
739 Membrane (GDM) filtration. *Water Res.* **47**:2085–2095.
740 Derlon N, Peter-Varbanets M, Scheidegger A, Pronk W, Morgenroth E. 2012. Predation influences the
741 structure of biofilm developed on ultrafiltration membranes. *Water Res.* **46**:3323–3333.
742 Dreszer C, Wexler A, Drusová S, Overdijk T, Zwijnenburg A, Flemming H-C, Kruithof JC,
743 Vrouwenvelder JS. 2014. In-situ biofilm characterization in membrane systems using optical
744 coherence tomography: formation, structure, detachment and impact of flux change. *Water Res.*
745 **67**:243–254.
746 Drexler W, Fujimoto JG. 2008. Optical Coherence Tomography: Technology and Applications. Ed. W
747 Drexler, James G Fujimoto 1st ed. Berlin, Heidelberg, New York: Springer-Verlag 1346 p.
748 Fercher AF, Drexler W, Hitzenberger CK, Lasser T. 2010. Optical coherence tomography –
749 development, principles, applications. *Reports Prog. Phys.* **20**:251–276.
750 Flemming H-C, Wingender J. 2010. The biofilm matrix. *Nat. Rev. Microbiol.* **8**:623–633.
751 Flemming H-C, Wingender J, Szewzyk U, Steinberg P, Rice SA, Kjelleberg S. 2016. Biofilms: an
752 emergent form of bacterial life. *Nat. Rev. Microbiol.* **14**:563–575.
753 Fortunato L, Bucs S, Linares RV, Cali C, Vrouwenvelder JS, Leiknes T. 2016a. Spatially-resolved in-
754 situ quantification of biofouling using optical coherence tomography (OCT) and 3D image

755 analysis in a spacer filled channel. *J. Memb. Sci.* **in press**.
756 Fortunato L, Jeong S, Wang Y, Behzad AR, Leiknes T. 2016b. Integrated approach to characterize
757 fouling on a flat sheet membrane gravity driven submerged membrane bioreactor. *Bioresour.*
758 *Technol.* **222**:335–343.
759 Fortunato L, Qamar A, Wang Y, Jeong S, Leiknes T. 2017. In-situ assessment of biofilm formation in
760 submerged membrane system using optical coherence tomography and computational fluid
761 dynamics. *J. Memb. Sci.* **521**:84–94.
762 Galy O, Latour-Lambert P, Zrelli K, Ghigo JM, Beloin C, Henry N. 2012. Mapping of bacterial
763 biofilm local mechanics by magnetic microparticle actuation. *Biophys. J.* **103**:1400–1408.
764 Gao Y, Haavisto S, Li W, Tang CY, Salmela J, Fane AG. 2014. Novel approach to characterizing the
765 growth of a fouling layer during membrane filtration via optical coherence tomography. *Environ.*
766 *Sci. Technol.* **48**:14273–14281.
767 Gao Y, Haavisto S, Tang CY, Salmela J, Li W. 2013. Characterization of fluid dynamics in spacer-
768 filled channels for membrane filtration using Doppler optical coherence tomography. *J. Memb.*
769 *Sci.* **448**:198–208.
770 Gjersing EL, Codd SL, Seymour JD, Stewart PS. 2005. Magnetic resonance microscopy analysis of
771 advective transport in a biofilm reactor. *Biotechnol. Bioeng.* **89**:822–834.
772 Graf von der Schulenburg D, Vrouwenvelder JS, Creber SA, van Loosdrecht M, Johns ML, Graf von
773 der Schulenburg DA, van Loosdrecht MCM. 2008. Nuclear magnetic resonance microscopy
774 studies of membrane biofouling. *J. Memb. Sci.* **323**:37–44.
775 Guelon T, Mathias JD, Stoodley P. 2011. Advances in Biofilm Mechanics. In: Flemming, H-C,
776 Wingender, J, Szewzyk, U, editors. *Biofilm Highlights* 5th ed. Berlin, Heidelberg: Springer-
777 Verlag, pp. 111–139.
778 Haberer CM, Rolle M, Liu S, Cirpka O a, Grathwohl P. 2011. A high-resolution non-invasive
779 approach to quantify oxygen transport across the capillary fringe and within the underlying
780 groundwater. *J. Contam. Hydrol.* **122**:26–39.
781 Haisch C, Niessner R. 2007. Visualisation of transient processes in biofilms by optical coherence
782 tomography. *Water Res.* **41**:2467–2472.
783 Halan B, Buehler K, Schmid A. 2012. Biofilms as living catalysts in continuous chemical syntheses.
784 *Trends Biotechnol.* **30**:453–465.
785 Hall-Stoodley L, Costerton JW, Stoodley P. 2004. Bacterial biofilms: from the natural environment to
786 infectious diseases. *Nat. Rev. Microbiol.* **2**:95–108.
787 Haralick RM, Shanmugam K, Dinstein I. 1973. Textural Features for Image Classification. *IEEE*
788 *Trans. Syst. Man. Cybern.* **3**:610–621.
789 Hell SW. 2007. Far-Field Optical Nanoscopy. *Science* **316**:1153–1158.
790 Hell SW. 2009. Microscopy and its focal switch. *Nat. Methods* **6**:24–32.
791 Herzberg M, Elimelech M. 2007. Biofouling of reverse osmosis membranes: Role of biofilm-

792 enhanced osmotic pressure. *J. Memb. Sci.* **295**:11–20.
793 Hijnen WAM, Castillo C, Brouwer-Hanzens a H, Harmsen DJH, Cornelissen ER, van der Kooij D.
794 2012. Quantitative assessment of the efficacy of spiral-wound membrane cleaning procedures to
795 remove biofilms. *Water Res.* **46**:6369–6381.
796 Horn H, Lackner S. 2014. Modeling of Biofilm Systems: A Review. Ed. Kai Muffler, Roland Ulber.
797 *Adv. Biochem. Engin./Biotechnol.*:53–76.
798 Hornemann JA, Codd SL, Fell RJ, Stewart PS, Seymour JD. 2009. Secondary flow mixing due to
799 biofilm growth in capillaries of varying dimensions. *Biotechnol. Bioeng.* **103**:353–360.
800 Hornemann J a, Lysova A a, Codd SL, Seymour JD, Busse SC, Stewart PS, Brown JR. 2008.
801 Biopolymer and water dynamics in microbial biofilm extracellular polymeric substance.
802 *Biomacromolecules* **9**:2322–2328.
803 Hoskins BC, Fevang L, Majors PD, Sharma MM, Georgiou G. 1999. Selective imaging of biofilms in
804 porous media by NMR relaxation. *J. Magn. Reson.* **139**:67–73.
805 Huang D, Swanson EA, Lin CP, Schuman JS, Stinson WG, Chang W, Hee MR, Flotte T, Gregory K,
806 Puliafito CA, Fujimoto JG. 1991. Optical Coherence Tomography. *Science* **254**:1178–1181.
807 Ivleva NP, Wagner M, Horn H, Niessner R, Haisch C. 2009. Towards a nondestructive Chemical
808 Characterization of Biofilm Matrix by Raman Microscopy. *Anal. Bioanal. Chem.* **393**:197–206.
809 Ivleva NP, Wagner M, Horn H, Niessner R, Haisch C. 2010a. Raman microscopy and surface-
810 enhanced Raman scattering (SERS) for in situ analysis of biofilms. *J. Biophotonics* **3**:548–556.
811 Ivleva NP, Wagner M, Szkola A, Horn H, Niessner R, Haisch C. 2010b. Label-Free in Situ SERS
812 Imaging of Biofilms. *J. Phys. Chem. B* **114**:10184–10194.
813 Joens MS, Huynh C, Kasuboski JM, Ferranti D, Sigal YJ, Zeitvogel F, Obst M, Burkhardt CJ, Curran
814 KP, Chalasani SH, Stern LA, Goetze B, Fitzpatrick JAJ. 2013. Helium Ion Microscopy (HIM)
815 for the imaging of biological samples at sub-nanometer resolution. *Sci. Rep.* **3**:1–7.
816 Kiperstok AC, Sebestyén P, Podola B, Melkonian M. 2017. Biofilm cultivation of Haematococcus
817 pluvialis enables a highly productive one-phase process for astaxanthin production using high
818 light intensities. *Algal Res.* **21**:213–222.
819 Kittler J, Illingworth J. 1986. Minimum error thresholding. *Pattern Recognit.* **19**:41–47.
820 Kittler J, Illingworth J, Föglein J. 1985. Threshold Selection Based on a Simple image Statistic.
821 *Comput. vision, Graph. image Process.* **30**:125–147.
822 Kniggendorf A-K, Nogueira R, Kelb C, Schadzek P, Meinhardt-Wollweber M, Ngezahayo A, Roth B.
823 2016. Confocal Raman microscopy and fluorescent in situ hybridization – A complementary
824 approach for biofilm analysis. *Chemosphere* **161**:112–118.
825 Kniggendorf A-K, Meinhardt-Wollweber M. 2011. Of microparticles and bacteria identification -
826 (resonance) Raman micro-spectroscopy as a tool for biofilm analysis. *Water Res.* **45**:4571–4582.
827 Körstgens V, Flemming HC, Wingender J, Borchard W. 2001. Influence of calcium ions on the
828 mechanical properties of a model biofilm of mucoid Pseudomonas aeruginosa. In: . *Water Sci.*

Technol., Vol. 43, pp. 49–57.

Kubryk P, Kölschbach JS, Marozava S, Lueders T, Meckenstock RU, Niessner R, Ivleva NP. 2015. Exploring the Potential of Stable Isotope (Resonance) Raman Microspectroscopy and Surface-Enhanced Raman Scattering for the Analysis of Microorganisms at Single Cell Level. *Anal. Chem.* **87**:6622–6630.

Kubryk P, Niessner R, Ivleva NP. 2016. The origin of the band at around 730 cm^{-1} in the SERS spectra of bacteria: a stable isotope approach. *Analyst* **141**:2874–2878.

Lawrence JR, Swerhone GDW, Leppard GG, Araki T, Zhang X, West MM, Hitchcock AP. 2003. Scanning Transmission X-Ray, Laser Scanning, and Transmission Electron Microscopy Mapping of Exopolymeric Matrix of Microbial Biofilms. *Appl. Environ. Microbiol.* **69**:5543–5554.

Lee JH, Lee NI, Kim SD. 1992. A fast and adaptive method to estimate texture statistics by the spatial gray level dependence matrix (SGLDM) for texture image segmentation. *Pattern Recognit. Lett.* **13**:291–303.

Li C, Wagner M, Lackner S, Horn H. 2016. Assessing the influence of biofilm surface roughness on mass transfer by combining optical coherence tomography and two-dimensional modeling. *Biotechnol. Bioeng.* **113**:989–1000.

Limbert G, Bryan R, Cotton R, Young P, Hall-stoodley L, Kathju S, Stoodley P. 2013. Acta Biomaterialia On the mechanics of bacterial biofilms on non-dissolvable surgical sutures : A laser scanning confocal microscopy-based finite element study **9**:6641–6652.

Lin GG, Scott JG. 2012. Imaging intracellular protein dynamics by spinning disk confocal microscopy. *Methods Enzymol.* **504**:293–313.

Lv Y, Ju K, Wang L, Sun T, Miao R, Wang X, Wei F, Xia S. 2015. In situ probing of microbial activity within anammox granular biomass with microelectrodes. *J. Biosci. Bioeng.* **online**.

Manz B, Volke F, Goll D, Horn H. 2005. Investigation of biofilm structure, flow patterns and detachment with magnetic resonance imaging. *Water Sci. Technol.* **52**:1–6.

Manz B, Volke F, Goll D, Horn H. 2003. Measuring Local Flow Velocities and Biofilm Structure in Biofilm Systems With Magnetic Resonance Imaging (MRI). *Biotechnol. Bioeng.* **84**:424–432.

Martin KJ, Bolster D, Derlon N, Morgenroth E, Nerenberg R. 2014. Effect of fouling layer spatial distribution on permeate flux: A theoretical and experimental study. *J. Memb. Sci.* **471**:130–137.

Mathias JD, Stoodley P. 2009. Applying the digital image correlation method to estimate the mechanical properties of bacterial biofilms subjected to a wall shear stress. *Biofouling* **25**:695–703.

McLean JS, Ona ON, Majors PD. 2008. Correlated biofilm imaging, transport and metabolism measurements via combined nuclear magnetic resonance and confocal microscopy. *ISME J.* **2**:121–131.

Milferstedt K, Pons M-NN, Morgenroth E. 2008a. Analyzing characteristic length scales in biofilm

structures. *Biotechnol. Bioeng.* **102**:368–379.
Milferstedt K, Pons MN, Morgenroth E. 2008b. Textural fingerprints: A comprehensive descriptor for biofilm structure development. *Biotechnol. Bioeng.* **100**:889–901.
Minsky M. 1988. Memoir on Inventing the Confocal Scanning Microscope. *Scanning* **10**:128–138.
Morgenroth E, Milferstedt K. 2009. Biofilm engineering: linking biofilm development at different length and time scales. *Rev. Environ. Sci. Biotechnol.* **8**:203–208.
Murga R, Stewart PS, Daly D. 1995. Quantitative analysis of biofilm thickness variability. *Biotechnol. Bioeng.* **45**:503–510.
Neu TR, Lawrence JR. 2015. Innovative techniques, sensors, and approaches for imaging biofilms at different scales. *Trends Microbiol.* **23**:233–242.
Neu TR, Lawrence JR. 2014. Investigation of Microbial Biofilm Structure by Laser Scanning Microscopy. *Adv. Biochem. Eng. Biotechnol.*
Neu TR, Manz B, Volke F, Dynes JJ, Hitchcock AP, Lawrence JR. 2010. Advanced imaging techniques for assessment of structure, composition and function in biofilm systems. *FEMS Microbiol. Ecol.* **72**:1–21.
Neugebauer U, Rösch P, Schmitt M, Popp J, Julien C, Rasmussen A, Budich C, Deckert V. 2006. On the way to nanometer-sized information of the bacterial surface by tip-enhanced Raman spectroscopy. *J. Chem. Phys. Phys. Chem.* **7**:1428–1430.
Nguyen T, Roddick F a, Fan L. 2012. Biofouling of water treatment membranes: a review of the underlying causes, monitoring techniques and control measures. *Membranes (Basel).* **2**:804–840.
Nielsen PH, Daims H, Lemmer H. 2009. FISH Handbook for Biological Wastewater Treatment: Identification and Quantification of Microorganisms in Activated Sludge and Biofilms by FISH. New York: IWA Publishing 123 p.
Nott KP, Heese FP, Hall LD, Macaskie LE, Paterson-Beedle M. 2005. Measurement of flow field in biofilm reactors by 3-D magnetic resonance imaging. *AIChE J.* **51**:3072–3079.
Nowicki B. 1985. Multiparameter representation of surface roughness. *Wear* **102**:161–176.
Otsu N. 1979. A threshold selection method from gray-level histograms. *IEEE Trans. Syst. Man. Cybern.* **SMC-9**:62–66.
Pätzold R, Keuntje M, Anders-von Ahlften A. 2006. A new approach to non-destructive analysis of biofilms by confocal Raman microscopy. *Anal. Bioanal. Chem.* **386**:286–292.
Pawley JB. 2006. Handbook of Biological Confocal Microscopy. Ed. James B Pawley. New York: Springer-Verlag 988 p.
Peter-Varbanets M, Hammes F, Vital M, Pronk W. 2010. Stabilization of flux during dead-end ultra-low pressure ultrafiltration. *Water Res.* **44**:3607–16.
Peterson BW, He Y, Ren Y, Zerdoum A, Libera MR, Sharma PK, van Winkelhoff AJ, Neut D, Stoodley P, van der Mei HC, Busscher HJ. 2015. Viscoelasticity of biofilms and their recalcitrance to mechanical and chemical challenges. *FEMS Microbiol. Rev.* **39**:234–245.

Picioreanu C, van Loosdrecht MC, Heijnen JJ. 1998. Mathematical modeling of biofilm structure with a hybrid differential-discrete cellular automaton approach. *Biotechnol. Bioeng.* **58**:101–116.

Pons MN, Milferstedt K, Morgenroth E. 2008. Macrostructural biofilm characterization via textural image analysis by SGLDM and GLRLM. In: . *IFAC Proc. Vol.* IFAC, Vol. 17, pp. 6675–6680.

Priester JH, Horst AM, Van de Werfhorst LC, Saleta JL, Mertes LA, Holden PA. 2007. Enhanced visualization of microbial biofilms by staining and environmental scanning electron microscopy. *J. Microbiol. Methods* **68**:577–587.

Ramanan B, Holmes WM, Sloan WT, Phoenix VR. 2010. Application of Paramagnetically Tagged Molecules for Magnetic Resonance Imaging of Biofilm Mass Transport Processes. *Appl. Environ. Microbiol.* **76**:4027–4036.

Rasmussen K, Reilly C, Li Y, Jones RS. 2016. Real-time imaging of anti-biofilm effects using CP-OCT. *Biotechnol. Bioeng.* **113**:198–205.

Ratheesh Kumar M, Murukeshan VM, Seah LK, Shearwood C. 2015. Quantification of biofilm thickness using a swept source based optical coherence tomography system. *Proc. SPIE* **9524**:1–6.

Reith F, Fairbrother L, Nolze G, Wilhelmi O, Clode PL, Gregg A, Parsons JE, Wakelin S a., Pring A, Hough R, Southam G, Brugger J. 2010. Nanoparticle factories: Biofilms hold the key to gold dispersion and nugget formation. *Geology* **38**:843–846.

Renslow RS, Babauta JT, Majors PD, Mehta HS, Ewing RJ, Ewing TW, Mueller KT, Beyenal H. 2014. A biofilm microreactor system for simultaneous electrochemical and nuclear magnetic resonance techniques. *Water Sci. Technol.* **69**:966–973.

Santi PA. 2011. Light sheet fluorescence microscopy: a review. *J. Histochem. Cytochem.* **59**:129–138.

Sarkar S, Mukherjee J, Roy D. 2009. Antibiotic production by a marine isolate (MS 310) in an ultra-low-speed rotating disk bioreactor. *Biotechnol. Bioprocess Eng.* **14**:775–780.

Saur T, Escudié R, Santa-Catalina G, Bernet N, Milferstedt K. 2016. Conservation of acquired morphology and community structure in aged biofilms after facing environmental stress. *Water Res.* **88**:164–172.

Saur T, Milferstedt K, Bernet N, Escudié R. 2014. An automated method for the quantification of moving predators such as rotifers in biofilms by image analysis. *J. Microbiol. Methods* **103**:40–43.

Schindelin J, Arganda-Carreras I, Frise E, Kaynig V, Longair M, Pietzsch T, Preibisch S, Rueden C, Saalfeld S, Schmid B, Tinevez J-Y, White DJ, Hartenstein V, Eliceiri K, Tomancak P, Cardona A. 2012. Fiji: an open-source platform for biological-image analysis. *Nat. Methods* **9**:676–682.

Schmitt J. 1999. Optical Coherence Tomography (OCT): A Review. *IEEE J. Sel. Top. Quantum Electron.* **5**:1205–1215.

Seymour JD, Codd SL, Gjersing EL, Stewart PS. 2004. Magnetic resonance microscopy of biofilm structure and impact on transport in a capillary bioreactor. *J. Magn. Reson.* **167**:322–327.

940 Shemesh H, Goertz DE, van der Sluis LWM, de Jong N, Wu MK, Wesselink PR. 2007. High
941 frequency ultrasound imaging of a single-species biofilm. *J. Dent.* **35**:673–678.
942 Shen Y, Huang C, Monroy GL, Janjaroen D, Derlon N, Lin J, Espinosa-Marzal R, Morgenroth E,
943 Boppart SA, Ashbolt NJ, Liu WT, Nguyen TH. 2016. Response of Simulated Drinking Water
944 Biofilm Mechanical and Structural Properties to Long-Term Disinfectant Exposure. *Environ. Sci.*
945 *Technol.* **50**:1779–1787.
946 Shen Y, Monroy GL, Derlon N, Janjaroen D, Huang C, Morgenroth E, Boppart SA, Ashbolt NJ, Liu
947 WT, Nguyen TH. 2015. Role of biofilm roughness and hydrodynamic conditions in legionella
948 pneumophila adhesion to and detachment from simulated drinking water biofilms. *Environ. Sci.*
949 *Technol.* **49**:4274–4282.
950 Shotton DM. 1989. Confocal scanning optical microscopy and its applications for biological
951 specimens. *J. Cell Sci.* **94**:175–206.
952 Siddiqui A, Farhat N, Bucs SS, Linares RV, Picioreanu C, Kruithof JC, Van Loosdrecht MCM,
953 Kidwell J, Vrouwenvelder JS. 2016. Development and characterization of 3D-printed feed
954 spacers for spiral wound membrane systems. *Water Res.* **91**:55–67.
955 Singer G, Besemer K, Schmitt-Kopplin P, Hödl I, Battin TJ. 2010. Physical heterogeneity increases
956 biofilm resource use and its molecular diversity in stream mesocosms. *PLoS One* **5**:1–11.
957 Singh RP, Shukla MK, Mishra A, Kumari P, Reddy CRK, Jha B. 2011. Isolation and characterization
958 of exopolysaccharides from seaweed associated bacteria Bacillus licheniformis. *Carbohydr.*
959 *Polym.* **84**:1019–1026.
960 Staal M, Borisov SM, Rickelt LF, Klimant I, Kühl M. 2011. Ultrabright planar optodes for
961 luminescence life-time based microscopic imaging of O2 dynamics in biofilms. *J. Microbiol.*
962 *Methods* **85**:67–74.
963 Staudt C, Horn H, Hempel DC, Neu TR. 2003. Screening of lectins for staining lectin-specific
964 glycoconjugates in the EPS of biofilms. In: O'Flaherty, V, Moran, P, Lens, P, Stoodley, P,
965 editors. *Biofilms Ind. Med. Environ. Biotechnol.* London: IWA Publishing, pp. 308–327.
966 Stewart PS. 2012. Mini-review: Convection around biofilms. *Biofouling* **28**:187–198.
967 Taherzadeh D, Picioreanu C, Horn H. 2012. Mass transfer enhancement in moving biofilm structures.
968 *Biophys. J.* **102**:1483–1492.
969 Taormina MJ, Jemielita M, Stephens WZ, Burns AR, Troll J V., Parthasarathy R, Guillemin K. 2012.
970 Invastigating Bacterial-Animal Symbioses with Light Sheet Microscopy. *Biol. Bull.* **223**:7–20.
971 Valladares Linares R, Wexler AD, Bucs SS, Dreszer C, Zwijnenburg A, Flemming H-C, Kruithof JC,
972 Vrouwenvelder JS. 2016. Compaction and relaxation of biofilms. *Desalin. Water Treat.*
973 **57**:12902–12914.
974 Valladares Linares R, Bucs SS, Li Z, AbuGhdeeb M, Amy G, Vrouwenvelder JS. 2014. Impact of
975 spacer thickness on biofouling in forward osmosis. *Water Res.* **57**:223–233.
976 Vrouwenvelder JS, Graf von der Schulenburg D a, Kruithof JC, Johns ML, van Loosdrecht MCM.

977 2009. Biofouling of spiral-wound nanofiltration and reverse osmosis membranes: a feed spacer
978 problem. *Water Res.* **43**:583–594.
979 Wagner M, Ivleva NP, Haisch C, Niessner R, Horn H. 2009. Combined use of confocal laser scanning
980 microscopy (CLSM) and Raman microscopy (RM): investigations on EPS-Matrix. *Water Res.*
981 **43**:63–76.
982 Wagner M, Manz B, Volke F, Neu TR, Horn H. 2010a. Online assessment of biofilm development,
983 sloughing and forced detachment in tube reactor by means of magnetic resonance microscopy.
984 *Biotechnol. Bioeng.* **107**:172–181.
985 Wagner M, Taherzadeh D, Haisch C, Horn H. 2010b. Investigation of the mesoscale structure and
986 volumetric features of biofilms using optical coherence tomography. *Biotechnol. Bioeng.*
987 **107**:844–853.
988 Wangpraseurt D, Wentzel C, Jacques SL, Wagner M, Kühl M. In vivo imaging of coral tissue and
989 skeleton with optical coherence tomography. *bioRxiv*:doi:10.1101/088682.
990 Ward BW, Notte JA, Economou NP. 2006. Helium ion microscope: A new tool for nanoscale
991 microscopy and metrology. *J. Vac. Sci. Technol. B Microelectron. Nanom. Struct.* **24**:2871–
992 2874.
993 Weiss N, van Leeuwen TG, Kalkman J. 2015. Simultaneous and localized measurement of diffusion
994 and flow using optical coherence tomography. *Opt. Express* **23**:3448.
995 Weiss N, Van Leeuwen TG, Kalkman J. 2013. Localized measurement of longitudinal and transverse
996 flow velocities in colloidal suspensions using optical coherence tomography. *Phys. Rev. E - Stat.*
997 *Nonlinear, Soft Matter Phys.* **88**:1–7.
998 Weiss N, el Tayeb el Obied K, Kalkman J, Lammertink RGH, van Leeuwen TG. 2016. Measurement
999 of biofilm growth and local hydrodynamics using optical coherence tomography. *Biomed. Opt.*
1000 *Express* **7**:3508–3518.
1001 West S, Horn H, Hijnen W, Castillo C, Wagner M. 2014. Confocal laser scanning microscopy as a
1002 tool to validate the efficiency of membrane cleaning procedures to remove biofilms. *Sep. Purif.*
1003 *Technol.* **122**:402–411.
1004 West S, Wagner M, Engelke C, Horn H. 2016. Optical coherence tomography for the in situ three-
1005 dimensional visualization and quantification of feed spacer channel fouling in reverse osmosis
1006 membrane modules. *J. Memb. Sci.* **498**:345–352.
1007 Wibisono Y, El Obied KE, Cornelissen ER, Kemperman AJB, Nijmeijer K. 2015. Biofouling removal
1008 in spiral-wound nanofiltration elements using two-phase flow cleaning. *J. Memb. Sci.* **475**:131–
1009 146.
1010 Wilderer PA, Characklis WG. 1989. Structure and Function of Biofilms. John Wiley & Sons, New
1011 York.
1012 Xavier JB, Schnell A, Wuertz S, Palmer R, White DC, Almeida JS. 2001. Objective threshold
1013 selection procedure (OTS) for segmentation of scanning laser confocal microscope images. *J.*

Microbiol. Methods **47**:169–180.

Xi C, Marks D, Schlachter S, Luo W, Boppart SA. 2006. High-resolution three-dimensional imaging of biofilm development using optical coherence tomography. *J. Biomed. Opt.* **11**:34001/1-6.

Yaqoob Z, Wu J, Yang C. 2005. Spectral domain optical coherence tomography: a better OCT imaging strategy. *Biotechniques* **39**:S6–S13.

Yawata Y, Uchiyama H, Nomura N. 2009. Visualizing the effects of biofilm structures on the influx of fluorescent material using combined confocal reflection and fluorescent microscopy. *Microbes Environ.* **25**:49–52.

Yerly J, Hu Y, Jones SM, Martinuzzi RJ. 2007. A two-step procedure for automatic and accurate segmentation of volumetric CLSM biofilm images. *J. Microbiol. Methods* **70**:424–433.

Figure captions

Figure 1: Scheme illustrating the definition of scales at which biofilm structure might be investigated. The definition of scales is not based on the resolution of the imaging techniques. Moreover, recent developments extended the capabilities of the methods shown here. Thus, methods might overlap in some cases. Image taken with permission from Wagner et al. (2010b) and modified for this review.

Figure 2: Scanning electron micrograph of a heterotrophic wastewater biofilm cultivated in a lab-scale flume. The network-like biofilm structure is visible although altered through dehydration. Scale bar = 20 µm.

Figure 3: Series of OCT B-Scans (xz-planes) along the y-axis of the C-scan (3D dataset) through heterotrophic biofilms grown at different hydrodynamic conditions. Size of a B-scan = 4 mm × 1.6 mm. Image taken with permission from Wagner et al. (2010b).

Figure 4: Calculated shear-rate in the B-scan for the transverse flow velocity component. The first row shows the shear-rate in the y-direction and the second row shows the shear-rate in the z-direction. The first column shows the reference data, and the second and third column show the data after 24 and 48 hours after starting the experiment, respectively. All data refer to OCT measurements. Image taken with permission from Weiss et al. (2016).

Figure 5: The scheme compares different binarization approaches. The raw imaging dataset (B-scan) contains a structure (rectangle) including a SNR drop-off of 20 (intensity gradient). For elucidation purposes there is no noise (black background). The red-dashed frame in (A) outlines the object. As shown in (A), different thresholding algorithms can result in different amounts of pixels assigned to the foreground (white) in the binary dataset. In (B) a procedure is proposed which compensates for the SNR drop-off present in OCT datasets acquired with spectrometer-based devices. A C-scan composed of identical B-scans (raw image, xz-plane) is assumed, which is resliced into a stack of xy-planes. The scheme includes only three xy-planes with an SNR of 20 (blue), 10 (green), and 5 (red). For each individual xy-plane the threshold is calculate using Otsu's method (Otsu, 1979). The binary stack of xy-planes is resliced into a series of xz-planes (C-scan). Independent of the SNR ratio of a particular xy-plane, Otsu's thresholding method assigned the complete object correctly to the foreground. Results of (A) using the triangle method and (B) using Otsu's method are equal in this particular example.

Figure 6: Calculation of porosity. (A) depicts the calculation of global porosity. (B) and (C) illustrate the calculation of biofilm porosity. In (B) background signals *vx(0)* outside the biofilm structure are ignored. Through bending of the biofilm structure in (C), the biofilm porosity is overestimated by the number of additional background signals *vx(0)* within the gray region.

Figure 7: Proposed scheme of the extraction of the bulk-biofilm interface from OCT C-scans for the analysis of the biofilm topography. The biofilm topography is generated by assigning the distance h_i of a particular xy-plane from the substratum to the target 3D stack (see Eq. 9). Thereby, the stack becomes depth-coded. By calculating the maximum intensity projection the topography of the bulk-biofilm interface is represented in 2D. Calibration bars indicate the grayscale intensity. For the binary datasets it is 0 or 255 whereas it is in a range of 0 to 10.0 for the depth-coded xy-planes as well as for the final maximum intensity projection.

Figure 8: OCT B-scans of the biofilm deformation as a function of the shear stress from the beginning and the end of an experiment. (A) shows the OCT B-scan at the begin (shear stress = 0.01 Pa) and (B) at the end of the deformation experiment at a shear stress of 1.64 Pa. The filamentous structure elongated (ΔL = 220 µm). Simultaneously a change of the angle of deformation α was observed. Scale bar equals 250 µm. Flow from left to right. Image taken with permission from Blauert et al. (2015).

Figure 9: OCT images of a biofilm structure at constant flow velocity (0.1 m/s) but changing permeate flux. The permeate flux is 20 L/(m²h) for the right image 60 L/(m²h) for the middle image and again 20 L/(m²h) for the left image. Image taken with permission from Valladares Linares et al. (2015).

Figure 10: An OCT biofilm image used to simulate the permeate flux (m/s) through membrane (white lower region) and biofilm. The lowest flux (blue) can be found below cavities in the biofilm due a certain pressure loss in direction of the membrane. Image taken with permission from Fortunato et al. (2017).

1083 Figure 1

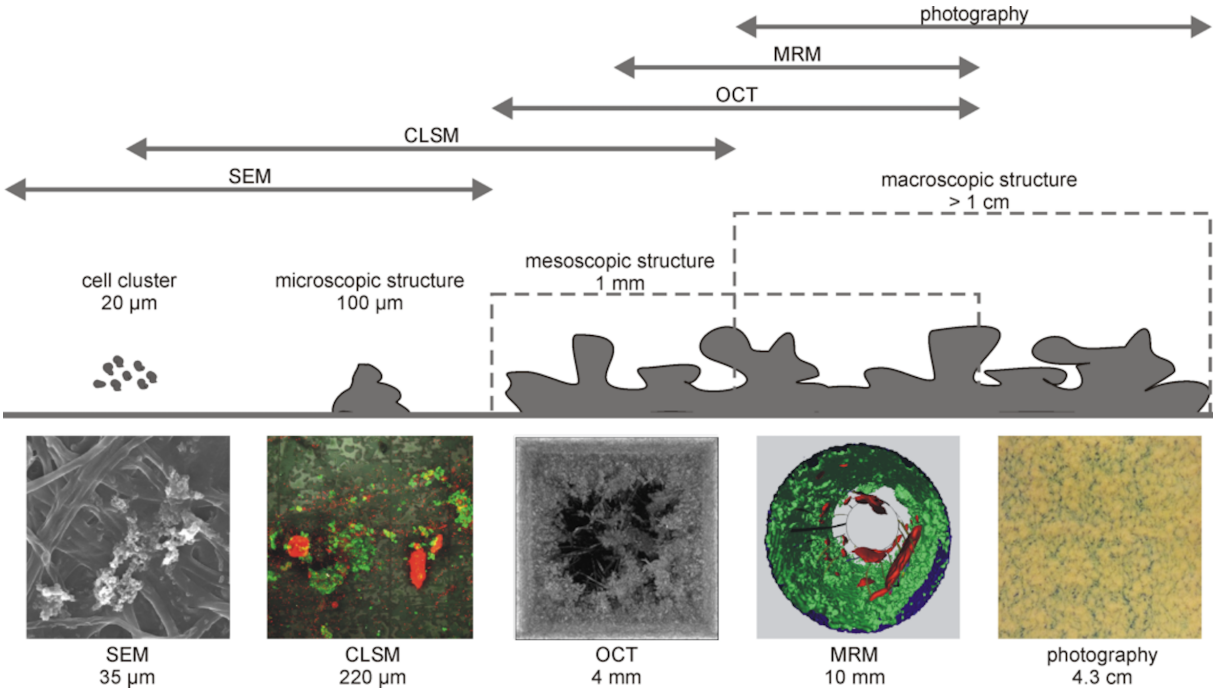

1084

1085

1086 Figure 2

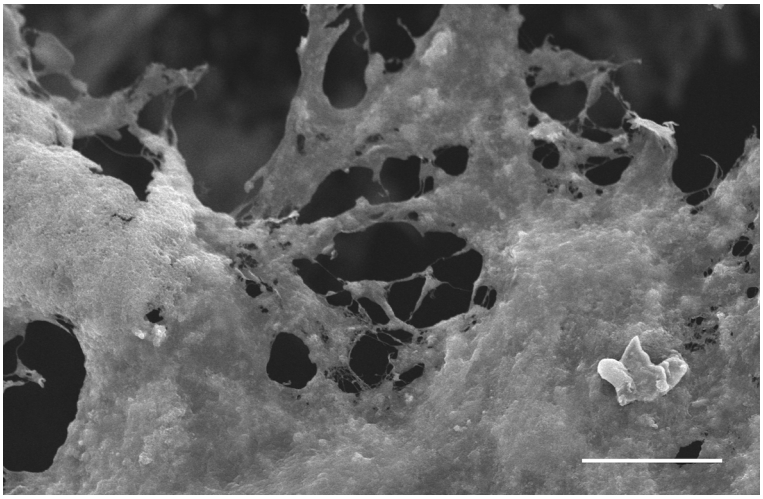

1087

1088

1089 Figure 3

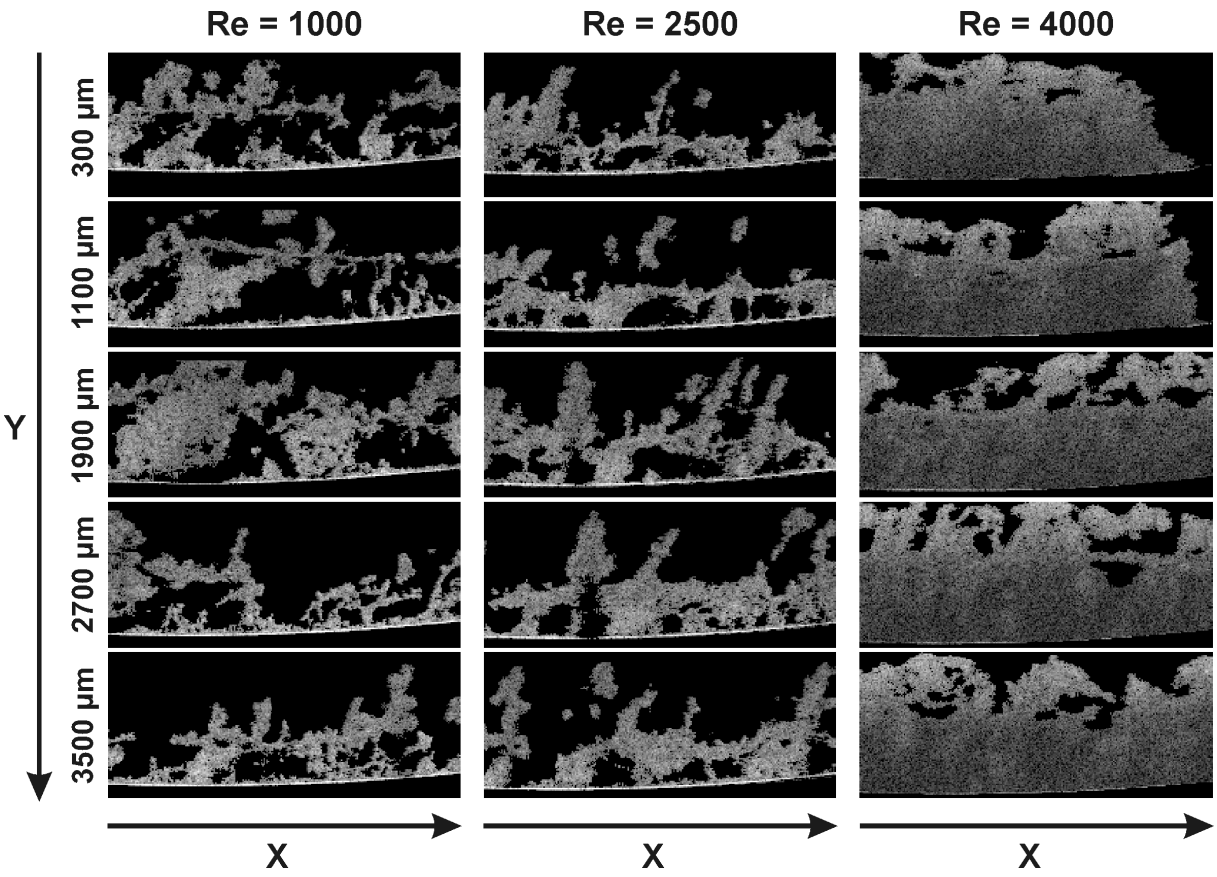

1090

1091

1092 Figure 4

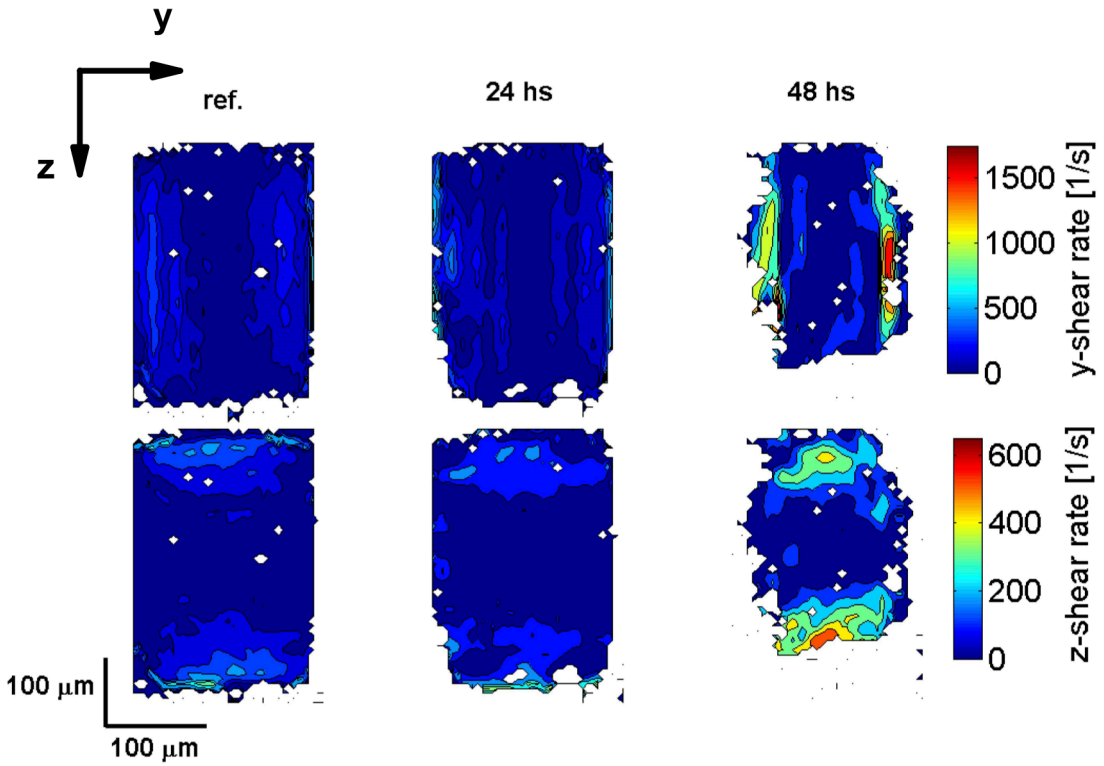

1093

1094

Figure 5

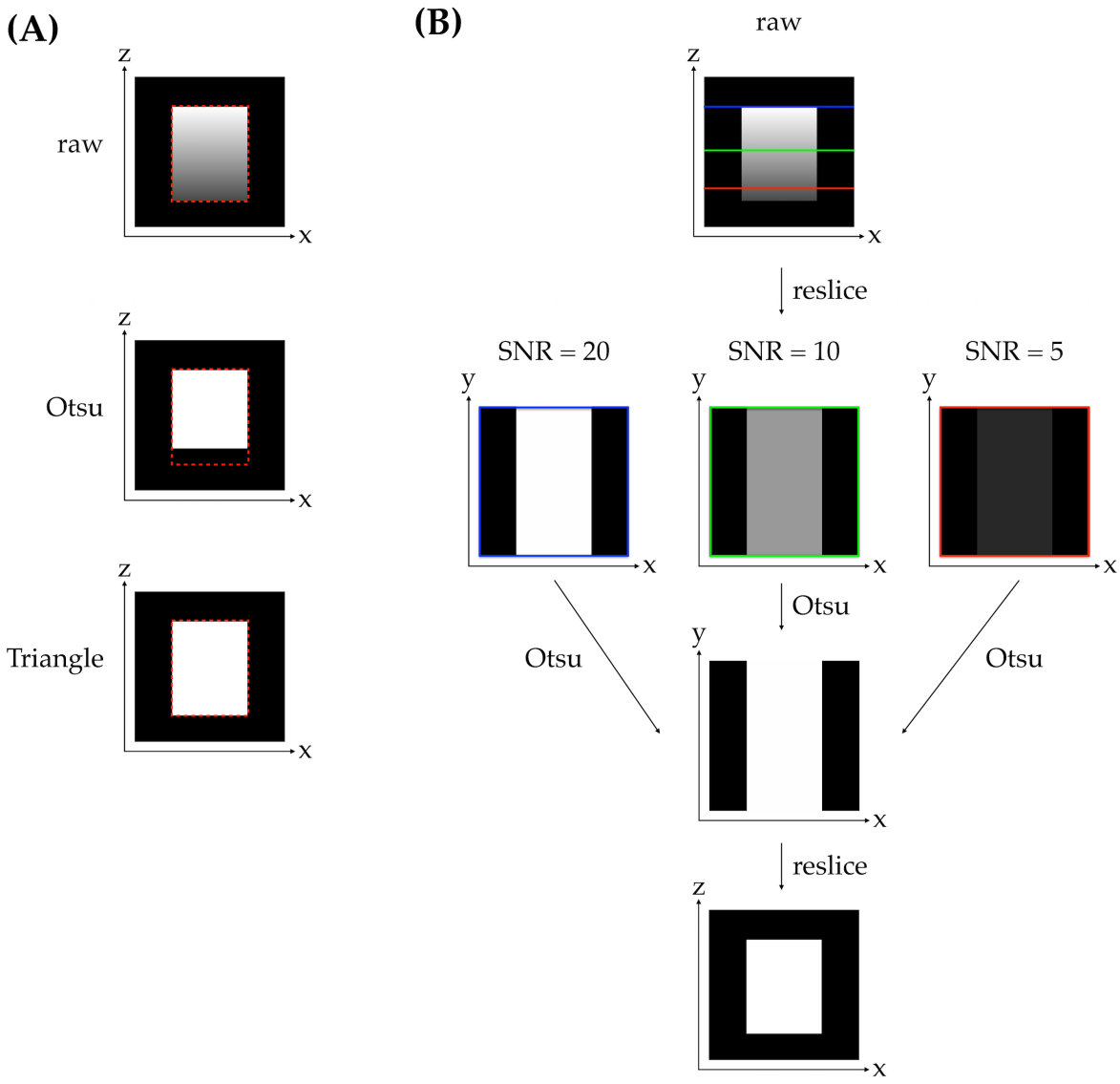
(A)
raw
Otsu
Triangle
z
x
(B)
raw
reslice
SNR = 20
SNR = 10
SNR = 5
y
Otsu
Otsu
Otsu
reslice

Figure 6

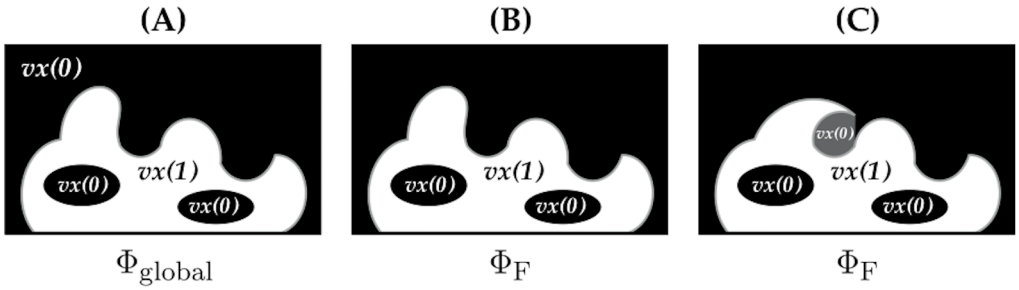
(A)
(B)
(C)
vx(0)
vx(0)
vx(1)
vx(0)
vx(0)
vx(1)
vx(0)
vx(0)
vx(0)
vx(1)
vx(0)
Φ_{global}
Φ_{F}
Φ_{F}

Figure 7

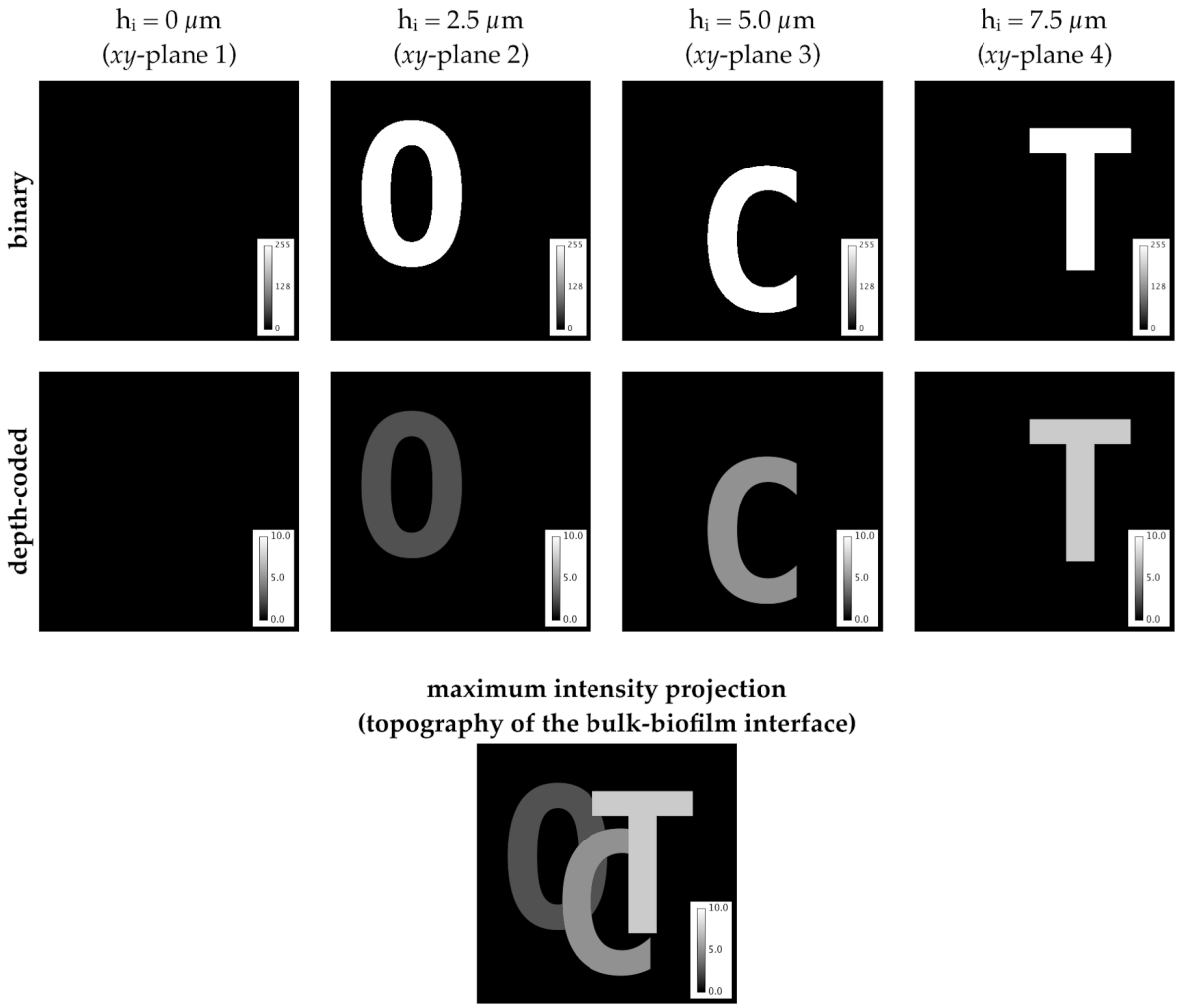
$h_i = 0\ \mu m$
(xy-plane 1)
$h_i = 2.5\ \mu m$
(xy-plane 2)
$h_i = 5.0\ \mu m$
(xy-plane 3)
$h_i = 7.5\ \mu m$
(xy-plane 4)
binary
depth-coded
255
128
0
10.0
5.0
0.0
maximum intensity projection
(topography of the bulk-biofilm interface)

1104 Figure 8

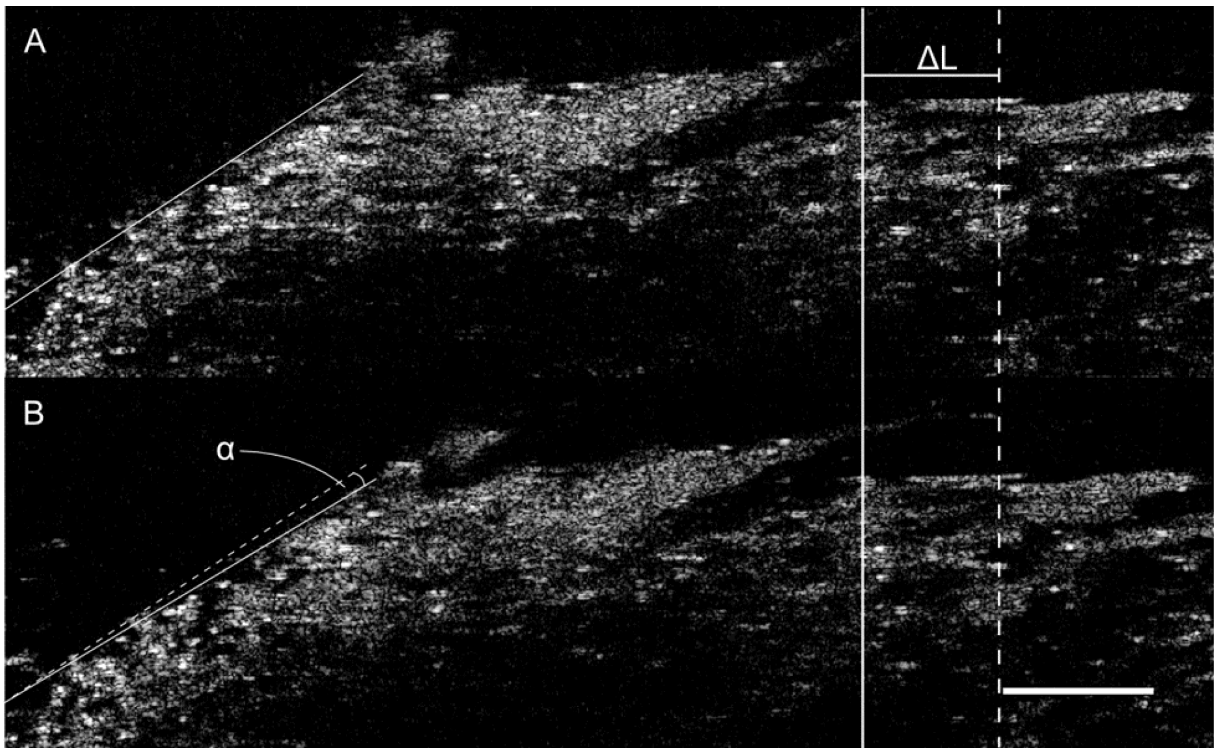

1105

1106

1107 Figure 9

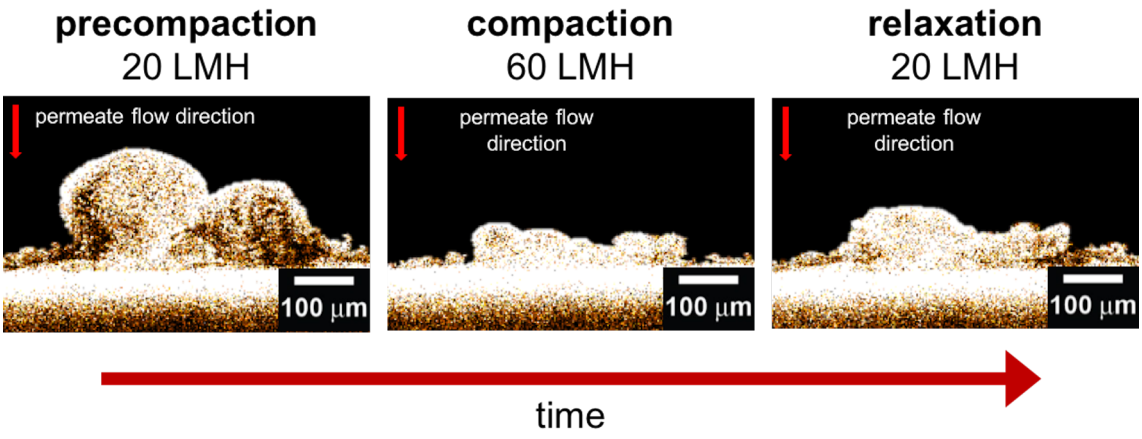

1108

1109

1110 Figure 10

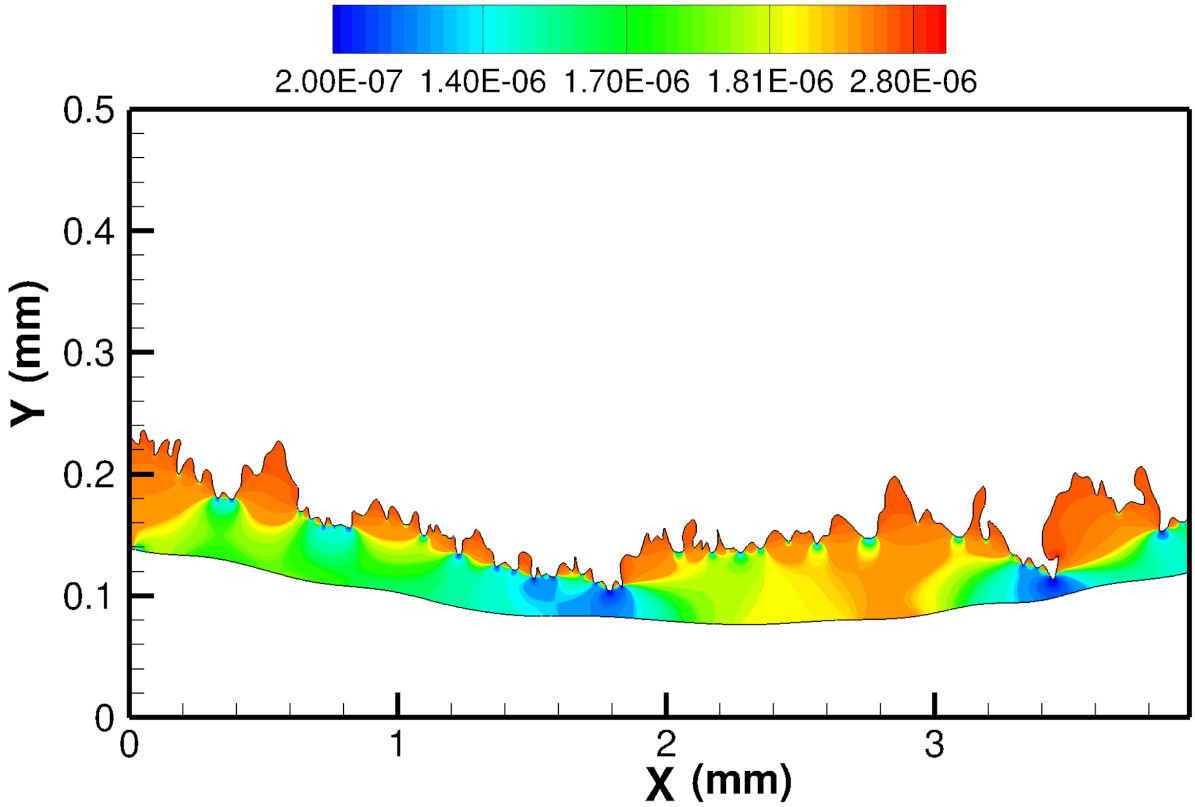

1111